Lab on a Chip

ROYAL SOCIETY OF CHEMISTRY

CRITICAL REVIEW

View Article Online
View Journal | View Issue

Cite this: *Lab Chip*, 2026, **26**, 1547

Structure-enabled liquid manipulation: bioinspired control across all dimensions

Siqi Sun,[a] Liqiu Wang *[ab] and Yiyuan Zhang *[a]

Received 29th August 2025,
Accepted 4th November 2025

DOI: 10.1039/d5lc00828j

rsc.li/loc

Directional liquid manipulation underpins critical processes across nature and engineering, where targeted functionality demands precise control over fluid behaviour. While fundamental theories for liquid manipulation are well-established, optimizing control along application-specific minimal-path trajectories remains a significant challenge. This review discusses recent advances in bioinspired strategies and engineered manipulators enabling superior liquid directional control across dimensional frameworks: 1D trajectories for targeted delivery, 2D planes for complex transport, and 3D spaces for programmable interfaces. Drawing on nature's energy-efficient principles, from Laplace pressure gradients to capillary effects, we decode evolutionary-optimized liquid manipulation mechanisms and their translation into dimension-specific artificial systems. These manipulators achieve precise liquid guidance through simplified asymmetric architectures, enhancing liquid utilization efficiency. Finally, we outline design paradigms for next-generation on-demand liquid control systems, bridging interfacial phenomena with microfluidic, thermal, and environmental technologies.

1. Introduction

Liquids are indispensable carriers of mass and energy in biological and industrial systems,[1–7] mediating vital transfer processes through interfacial interactions with gases, solids, or other liquids.[8–12] However, spatial separation between liquid sources and target phases often impedes direct exchange, necessitating directional spreading to bridge this gap. Uncontrolled isotropic spreading, driven by surface energy minimization, leads to significant resource loss. In addition, rapid vaporization under extreme conditions further limits liquid availability. Nature has evolved elegant solutions to these challenges: specialized structures in plants and animals enable directional transport,[13,14] efficient condensation,[15–17] and retention[18,19] of liquids with minimal energy consumption,[20,21] inspiring advanced liquid manipulation technologies.

Controlling liquid movement requires guiding it along defined one-dimensional (1D) trajectories under unbalanced

[a] *Department of Mechanical Engineering, The Hong Kong Polytechnic University, Hong Kong SAR, PR China. E-mail: liqiu.wang@polyu.edu.hk, yi-yuan.zhang@polyu.edu.hk*
[b] *Department of Biomedical Engineering, The Hong Kong Polytechnic University, Hong Kong SAR, PR China*

Siqi Sun

Siqi Sun received her bachelor's degree in Materials Science and Engineering from the Dalian University of Technology in 2020. She is currently a PhD candidate at the Department of Mechanical Engineering, The Hong Kong Polytechnic University. Her research interests include surface science, smart materials, biomimetics, and plant-based novel electronics.

Liqiu Wang

Liqiu Wang holds the Otto Poon Charitable Foundation Professorship in Smart and Sustainable Energy and serves as the Chair Professor of Thermal-Fluid and Energy Engineering at the Department of Mechanical Engineering, The Hong Kong Polytechnic University. Previously, he was a Chair Professor at the University of Hong Kong, where he contributed to both mechanical engineering and biomedical engineering. His research spans microfluidics, soft manufacturing, nonlinear computation, thermodynamics, fluid mechanics, and heat transfer.

forces (Fig. 1).[22] Natural systems have established specialised strategies for liquid directional control,[23–25] exemplified through asymmetric cones (Sarracenia,[26] cacti,[27] and pine needles[28]), capillary architectures (mouthparts of honeybees,[29,30] bats,[31,32] butterfly,[33] and hummingbirds[34]), and curvature morphology-facilitated deposition (*A. macrorrhiza*[35]). These enable horizontal, vertical upward, or vertical downward transport, which are fundamental directions that form the basis for complex pathways. Mimicking such strategies offers efficient solutions for fog harvesting,[36,37] oil–water separation,[38] water purification,[39] and precision irrigation,[40] minimizing residual loss *via* shortest-path transport.

Besides 1D, liquid manipulation extends to two-dimensional (2D) planes and three-dimensional (3D) space,[41] enabling sophisticated surface deformations and interfacial morphologies (Fig. 1). In 2D, liquids achieve multidirectional transport (*e.g.*, Araucaria[42] and *Crassula muscosa*[43]) or form controlled wetting patterns (*e.g.*, lotus leaf[44]). In 3D, structures like *T. capitata*[45] or plant vasculature[46] facilitate programmable transport and complex liquid–gas–solid interfaces, enhancing applications in biomedicine, thermal management, and antifouling.[47–53]

While existing reviews have extensively covered fundamental liquid control mechanisms[54–60] and external-field actuation (*e.g.*, electric, light, magnetic, thermal, acoustic, or pneumatic),[61–77] systematic optimization of transport pathways for application-specific efficiency remains relatively underexplored. Structure-guided strategies, energy-efficient and inherently scalable, offer distinct advantages for tailored directional control:[78] simplified 1D trajectories prove optimal for separation processes, whereas multidimensional (2D/3D) manipulation maximizes interfacial exchange in biochemical reactions,[79,80] thermal cooling,[81] or scenarios demanding precise interface regulation. To bridge this gap, our review first establishes the theoretical prerequisites for structural liquid control, and then lists bioinspired strategies and their underlying mechanisms evolved in nature. We subsequently highlight recent advances in structurally guided liquid manipulation across complexity scales—from foundational 1D trajectories to 2D open-channel planes and 3D spatial architectures—and conclude by addressing current limitations and future directions to advance application-driven liquid manipulator design.

Yiyuan Zhang

Yiyuan Zhang is an Assistant Professor at the Department of Mechanical Engineering, The Hong Kong Polytechnic University (PolyU). She obtained her Ph.D. in Mechanical and Materials Engineering from Western University, Canada. Before her current role, Prof. Zhang was a Research Assistant Professor at PolyU and a Postdoctoral Researcher at The University of Hong Kong. Her research encompasses soft and smart manufacturing, fluid structuring, additive manufacturing, microfluidics, and flexible electronics.

2. Basic principles of liquid manipulation

Effective liquid manipulation requires understanding of the interaction between liquid properties, solid surface characteristics, and the ambient environment.[82,83] This section outlines the fundamental mechanisms governing the liquid surface morphology and wetting dynamics, providing a theoretical foundation for designing solid structures that precisely control liquid behaviour under specific physicochemical conditions.

The cornerstone of modern wettability theory is Young's equation[84] (1805), which describes the equilibrium contact angle (θ) formed at the solid–liquid–vapor interface (Fig. 2a):[85]

$$\gamma_{LG}\cos\theta = \gamma_{SG} - \gamma_{SL} \quad (1)$$

where γ_{LG}, γ_{SG}, and γ_{SL} denote liquid–gas, solid–gas, and solid–liquid interfacial tensions, respectively. θ dictates a static droplet's morphology: hydrophobic surfaces ($\theta > 90°$) produce major-arc profiles, becoming near-spherical droplets on superhydrophobic surfaces ($\theta > 150°$). Conversely, hydrophilic surfaces ($\theta < 90°$) yield minor-arc shapes, advancing to near-flat films under superhydrophilic conditions ($\theta < 10°$).

Surface roughness fundamentally modulates wettability. Wenzel[86] (1936) and Cassie–Baxter[87] (1944) established models for rough surfaces (Fig. 2b and c). In the Wenzel state, liquid fully impregnates surface asperities:

$$\cos\theta_A = r\cos\theta \quad (2)$$

where θ_A is the apparent contact angle and r (roughness factor) is the ratio of the actual solid-surface area to its projected area. In the Cassie–Baxter state, air trapping creates composite interfaces where the droplet simultaneously makes contact with both solid and air phases:[88,89]

$$\cos\theta_A = \sigma_{SL}\cos\theta + (1 - \sigma_{SL})\cos 180° \quad (3)$$

Here, σ_{SL} is the solid–liquid fractional contact area. Strategically engineering micro/nano-scale roughness thus enables tunable wettability, enhancing the hydrophilicity/hydrophobicity of substrate materials to achieve extreme wetting states.[90,91]

Liquid dynamics manifest as two key modes: (i) liquid-over-solid wetting: governed by contact angle hysteresis

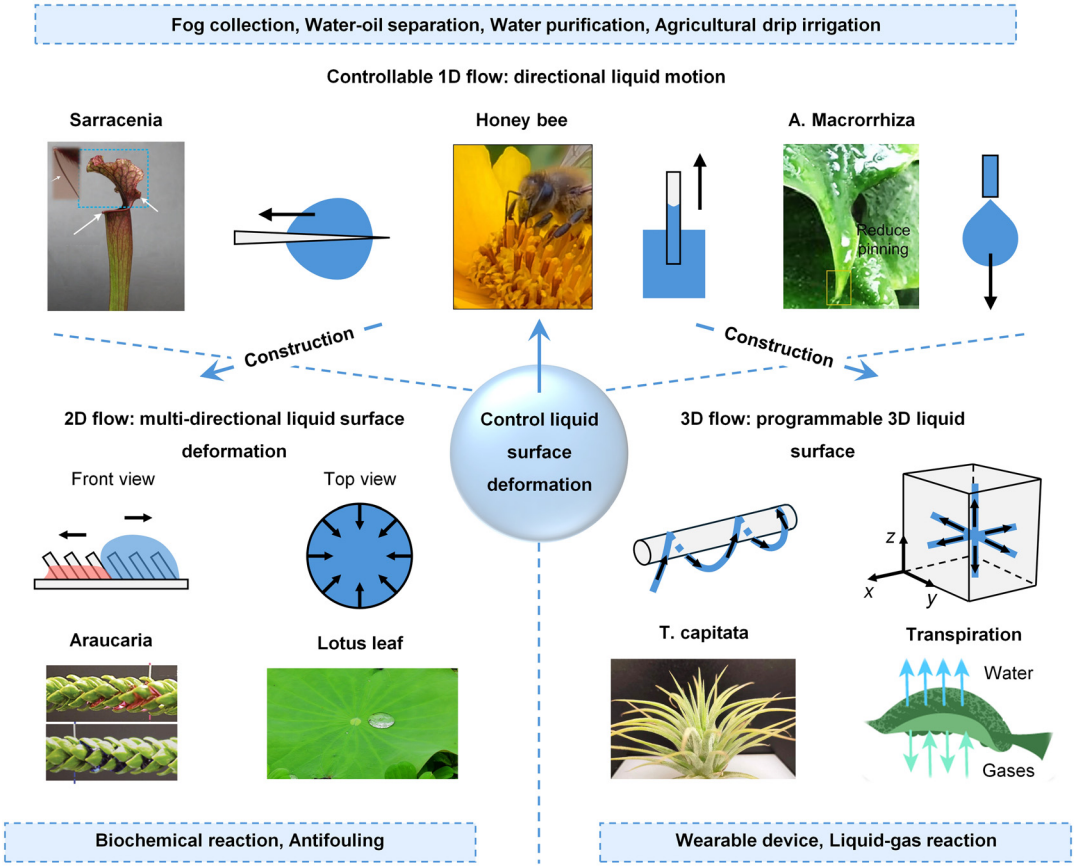

Fig. 1 Overview of primary controllable liquid behaviours learned from biological strategies, categorized as controlled motion in 1D trajectories, 2D planes, and 3D space, as well as their relationships and suitable application scenarios. The foundational control of liquid behaviour is to achieve unidirectional motion, termed controllable 1D flow, with primary directions including horizontal, vertical upward, and vertical downward. Representative biological structures enabling motion in these directions are Sarracenia trichomes (horizontal), honeybee mouthparts (vertical upward), and *A. macrorrhiza* leaves (vertical downward). Controllable 1D flow is ideal for applications requiring directional liquid transport along the shortest trajectories to minimize residual loss, such as fog collection, water–oil separation, water purification and irrigation. Controllable 1D flow constructs multi-directional liquid surface deformations in 2D planes and 3D space. Typical plants that enable macro multi-directional liquid transport and apply multi-directional forces to liquid surfaces in 2D planes are Araucaria and lotus leaves. Such controllable 2D flow is suitable for applications demanding adequate mass and energy exchange. 3D liquid manipulation achieved in nature is through specialized plant structures like *T. capitata*, which enables 3D liquid transport trajectories and physiological processes such as transpiration that facilitates complex liquid–solid–gas interface formation. These controllable 3D flow systems are particularly valuable for applications requiring sophisticated liquid–environment interaction. The Sarracenia image is reprinted with permission from ref. 26. Copyright 2018, Springer Nature. The honey bee image is reprinted with permission from ref. 153. Copyright 2023, The American Association for the Advancement of Science. The *A. macrorrhiza* image is reprinted with permission from ref. 35. Copyright 2020, National Academy of Sciences. The Araucaria image is reprinted with permission from ref. 42. Copyright 2021, The American Association for the Advancement of Science. The lotus leaf image is reproduced under CC BY 4.0. The *T. capitata* image is reprinted with permission from ref. 45. Copyright 2025, National Academy of Sciences. The transpiration image is reprinted with permission from ref. 197. Copyright 2021, Springer Nature.

(CAH, $\Delta\theta$), quantified *via* the Furmidge model[92] using advancing (θ_a) and receding (θ_r) angles on inclined surfaces[93] (Fig. 2d):

$$\Delta\theta = \theta_a - \theta_r \quad (4)$$

(ii) liquid-into-solid wicking: driven by the capillary effect and surface tension, involving liquid penetration into porous or confined solid matrices. For liquid rising between plates intersecting at angle α_1 (Fig. 2e), the capillary height $h(x)$ is as follows:

$$h(x) = \frac{2\gamma\cos\theta}{\rho g x \alpha_1} \quad (5)$$

where γ, ρ, and g are the surface tension, density, and gravity, respectively.[94–96] This effect dominates in hydrophilic systems.[97–99]

Interfacial energy minimization governs liquid transfer between immiscible phases (*e.g.*, reagent aspiration from storage vials into reaction chambers).[100] Consider a cubic manipulator immersed in liquid 1 (Fig. 2f). System energy (E_1) depends on interfacial areas and tensions (σ_{ij}):

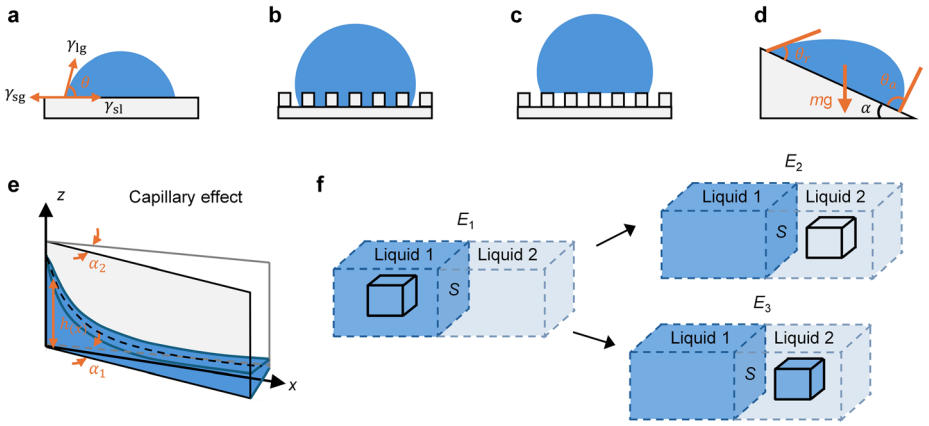

Fig. 2 Theoretical foundation of liquid wetting behaviour and determination of new liquid surface formation. (a) Schematic of the Young model. (b) Schematic of the Wenzel model. (c) Schematic of the Cassie–Baxter model. (d) Schematic of the Furmidge model. (e) Capillary effect in the gradient wedge corner. (f) Principle of minimum system energy governing the formation and rupture of liquid–liquid interfaces.

$$E_1 = S_S\sigma_{13} + S\sigma_{12} \quad (6)$$

Upon moving into liquid 2, complete displacement yields energy:

$$E_2 = S_S\sigma_{23} + S\sigma_{12} \quad (7)$$

Alternatively, captured liquid 1 creates new interfaces:

$$E_3 = S_{23}\sigma_{23} + S\sigma_{12} + S_{13}\sigma_{13} + S_{12}\sigma_{12} \quad (8)$$

Successful transfer occurs if $E_3 < E_2$, as the system evolves toward minimal energy.

3. Bioinspired liquid manipulation: evolutionary strategies in nature

Through evolutionary adaptation, organisms have developed sophisticated micro/nanostructures that optimize wettability and enable precise liquid control-essential adaptations for survival in diverse environments.

3.1. Wettability engineering for survival

Organisms precisely tailor surface wettability to address ecological challenges. Mobile animals typically evolve surfaces for locomotion and interaction, while sessile plants

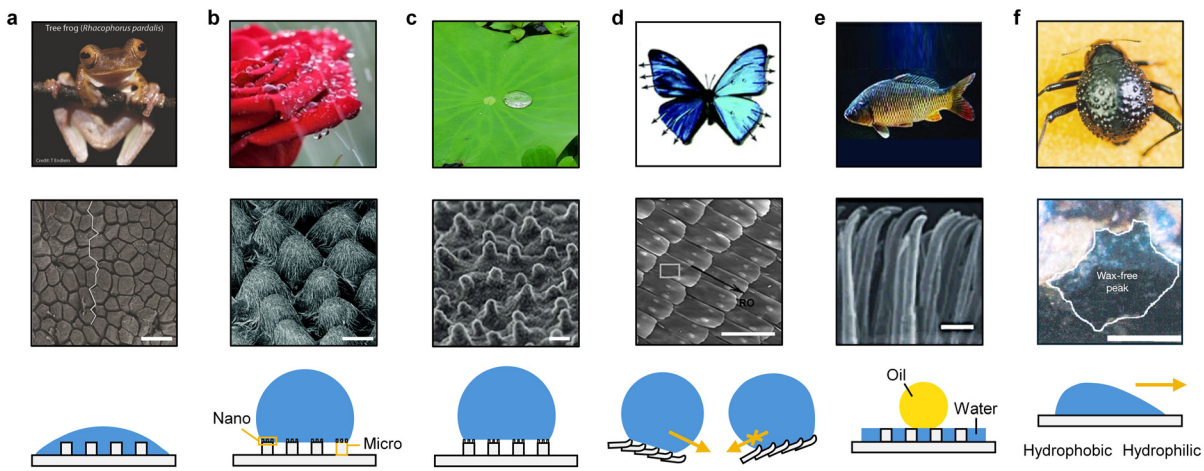

Fig. 3 Overview and mechanism schematic of typical natural organisms with specialized liquid manipulation strategies. (a) Tree frog. (b) Rose petal. (c) Lotus leaf. (d) Butterfly wing. (e) Fish scales. (f) Dessert beetle surface. The tree frog optical image and SEM image of (a) are reprinted with permission from ref. 101. Copyright 2015, Wiley. The rose petal optical image of (b) is reprinted with permission from ref. 24. Copyright 2025, Elsevier. The rose petal SEM image of (b) is reprinted with permission from ref. 104. Copyright 2008, American Chemical Society. The lotus leaf optical image of (c) is reproduced under CC BY 4.0. The lotus leaf SEM image of (c) is reprinted with permission from ref. 82. Copyright 2017, Springer Nature. The butterfly optical image and SEM image of (d) are reprinted with permission from ref. 33. Copyright 2005, The Royal Society of Chemistry. The fish optical image of (e) is reprinted with permission from ref. 24. Copyright 2025, Elsevier. The fish SEM image of (e) is reprinted with permission from ref. 114. Copyright 2013, Wiley. The desert beetle optical image and SEM image of (f) are reprinted with permission from ref. 115. Copyright 2001, Springer Nature.

develop defensive architectures against water loss, pathogens, or solar damage. Each solution reflects exquisite adaptation to specific biological constraints.

Tree frogs (Fig. 3a) leverage hydrophilic hierarchical toe pads to retain secreted liquid, establishing complete wetting on varied substrates. This generates robust adhesion for arboreal locomotion.[101] Roses (Fig. 3b) achieve paradoxical "sticky superhydrophobicity" through micropapillae with nanofolds.[102,103] While high static angles (>150°) minimize pathogen contact, nanoscale cavities create strong contact angle hysteresis (CAH), pinning droplets even when inverted (the "petal effect").[104,105] This reconciles disease resistance with water acquisition needs. Lotus leaves (Fig. 3c) employ superhydrophobicity for complete repellency.[106–108] Wax-coated microcapillaries and nanotubules[109,110] create a composite air–liquid interface, enabling near-spherical droplets with ultra-low CAH. This prevents water adhesion—critical for avoiding sunlight-focused thermal damage ("lensing effect") in aquatic habitats. Morpho butterfly wings (Fig. 3d) dynamically regulate wettability. Anisotropic micro/nanostructures enable reversible switching: outward tilting reduces solid–liquid contact for easy roll-off, while inward positioning engages flexible nanotips to increase adhesion—an active defense against rain/dew in tropical climates.[111]

Aquatic and arid specialists further demonstrate nature's ingenuity: fish skin (Fig. 3e) exhibits unique submerged amphiphilicity. Hierarchical scales of hydrophilic calcium proteins, phosphates, and mucus[112] form directional micropillars. In water, trapped interfacial layers create an oil–water–solid composite interface, yielding superoleophobicity for drag reduction and contaminant repellence ("underwater superoleophobicity").[113,114] Desert beetles (Fig. 3f) harvest water *via* spatially patterned wettability.[115] Their back features hydrophilic (wax-free, smooth bumps) and superhydrophobic (wax-coated, microstructured valleys) regions. In head-standing posture, fog nucleates on hydrophilic zones, grows, and rolls down hydrophobic channels to the mouth—enabling survival under hyperarid conditions.

These adaptations showcase nature's mastery in tailoring surface wettability for targeted liquid control. Besides surface phenomena, biological systems have also evolved sophisticated internal strategies for precise liquid management. For instance, plant leaves[116] exhibit structurally optimized vascular networks that prevent gas embolism during drought, thereby ensuring continuous water supply. This mechanism represents a distinct strategy for efficient water utilization in harsh environments. Together with surface-wettability-based control, these strategies collectively provide a rich design lexicon for advanced bioinspired technologies.

3.2. Biological asymmetric surface structures for directional liquid control

Asymmetric surface architectures represent nature's sophisticated solution for directional liquid transport, leveraging structural anisotropies across scales to break interfacial symmetry. These evolved geometries harness energy gradient, Laplace pressure gradient, the capillary effect, and the contact line pinning effect to guide liquid transport along predetermined pathways with remarkable efficiency.

Spider silk (Fig. 4a) exemplifies this principle through its periodic spindle-knot structures. Its complex hierarchical architecture comprises layered hydrophilic flagelliform proteins exhibiting humidity sensitivity.[117–123] The alternating roughness between knots and joints creates diameter variations of spider silk and establishes a surface energy gradient. Rougher spindle knots possess higher surface energy (lower contact angles) compared to joints. When droplets condense on the silk, an imbalance in water–substrate interfacial tension across the three-phase contact line generates a net driving force (F) that propels droplets toward the more wettable spindle knots:[120]

$$F = \int_{l_i}^{l_k} \gamma(\cos\theta_a - \cos\theta_r)\mathrm{d}l \tag{9}$$

where $\mathrm{d}l$ quantifies the distance between hydrophobic (l_i) and hydrophilic (l_k) zones. Similar gradients from chemical heterogeneity also direct droplet transport through energy gradients.[124,125]

Cactus is a highly drought-resistant tropical plant that has evolved specialized morphological adaptations to thrive in arid environments (Fig. 4b). This plant efficiently harvests water from fog through an integrated system of hierarchical surface structures, featuring a regular array of needle-like spines and hair-like trichome clusters. Each spine has three functionally distinct regions: a barbed tip for droplet nucleation, a grooved mid-section with a gradient morphology for directional transport, and a base with belt-structured trichomes for water absorption. This sophisticated architecture enables fog collection through Laplace pressure gradients,[126] where the conical geometry of the spines creates a pressure difference (ΔP) across adhering droplets (Fig. 4b). The resulting pressure imbalance drives directional water transport, as described by the following relationship:[127]

$$\Delta P = -\int_{r_1}^{r_2} \frac{2\gamma}{(r + r_0)^2}\sin\alpha\mathrm{d}z \tag{10}$$

where r represents the droplet radius, r_1 and r_2 denote the local radii of the conical column on opposite sides of the droplet, r_0 is the local radius of the conical structure, α is its half-apex angle, and $\mathrm{d}z$ describes the incremental radius change along the column. Due to the conical geometry, the Laplace pressure near the tip (r_1) exceeds that at the base (r_2), creating the pressure gradient difference. This imbalance generates a net driving force that propels the droplet unidirectionally from the tip toward the base.

Nepenthes alata integrates two complementary fluid regulatory effects (Fig. 4c), *i.e.*, forward capillary-driven fluid propagation and posterior edge-pinning stabilization. The forward transport is enabled by sharp wedge-shaped

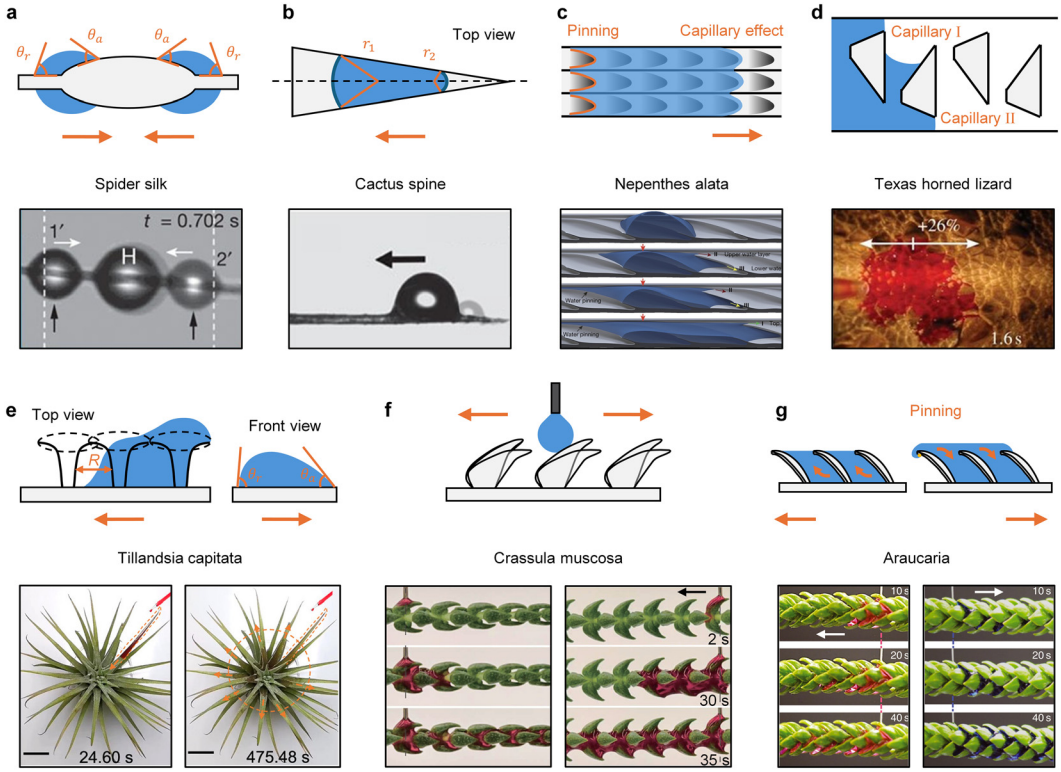

Fig. 4 Overview and mechanism schematic of directional liquid manipulation by organisms with asymmetric structures. (a) Spider silk. (b) Cactus spine. (c) *Nepenthes alata*. (d) Texas horned lizard. (e) *Tillandsia capitata*. (f) *Crassula muscosa*. (g) Araucaria. The spider silk image of (a) is reprinted with permission from ref. 123. Copyright 2010, Springer Nature. The cactus spine image of (b) is reprinted with permission from ref. 27. Copyright 2012, Springer Nature. The *Nepenthes alata* image of (c) is reprinted with permission from ref. 128. Copyright 2016, Springer Nature. The Texas horned lizard image of (d) is reprinted with permission from ref. 129. Copyright 2015, The Royal Society. The *Tillandsia capitata* image of (e) is reprinted with permission from ref. 45. Copyright 2025, National Academy of Sciences. The *Crassula muscosa* image of (f) is reprinted with permission from ref. 130. Copyright 2024, The American Association for the Advancement of Science. The Araucaria image of (g) is reprinted with permission from ref. 42. Copyright 2021, The American Association for the Advancement of Science.

microcavities formed between hydrophilic arched structures and microgroove bases, which generate a capillary hysteresis force, and the force can be modelled as capillary elevation (Fig. 2e). The natural system exhibits an evolved gradient morphology where the wedge angle progressively contracts from α_1 at the base to α_2 at the apex. The resulting gradient capillary rise $h_N(x)$ along the transport path follows this relationship:[128]

$$h_N(x) = \frac{2\gamma\cos\theta}{\rho g x \alpha_1} + \frac{\alpha_1 - \alpha_2}{\alpha_1 h_p}\frac{4\gamma^2\cos^2\theta}{\rho^2 g^2 x^2 {\alpha_1}^2} + \ldots \quad (11)$$

Here, h_p represents the height of the crossed plates. The superhydrophilic surface (contact angle $\theta \approx 0°$) exhibits a gradient wedge geometry where $\alpha_1 > \alpha_2$. Comparative analysis reveals that $h_N(x)_{\alpha_1>\alpha_2} > h_N(x)_{\alpha_1=\alpha_2}$, demonstrating that the narrowing microcavities along *Nepenthes alata*'s lip generate enhanced capillary action relative to uniform-wedge systems. This geometric optimization results in significantly accelerated liquid transport velocities.

The Texas horned lizard (Fig. 4d) harnesses capillary action, synergistically combining with Laplace pressure gradient, to direct water toward its snout through its evolved semi-open capillary channels.[129] The transport dynamics arise from the channels' saw-tooth periodicity, which creates asymmetric liquid surface curvature and consequently unbalanced Laplace pressures that preferentially drive forward flow twice as fast as reverse. Specifically, the lizard's skin features an interconnected network of shortened lateral capillaries that create continuous transport pathways. At capillary junctions, abrupt channel widening (*e.g.*, at capillary I) causes the advancing liquid meniscus curvature radius to approach infinity, temporarily halting forward motion. When liquid from adjacent capillary II reaches these junctions, it spontaneously redistributes into capillary I, propelling the liquid front forward until it encounters the next capillary II segment. This self-sustaining cycle of capillary refilling and meniscus regeneration reflects a critical adaptation for desert hydration.

Tillandsia capitata leaves integrate macroscale curvature with microscale trichomes for efficient directional liquid transport and spontaneous redistribution (Fig. 4e).[45] The transversely curved lanceolate macroscale morphology establishes fundamental liquid navigation pathways, and microscale hydrophilic trichomes provide capillary-driven water absorption. The density gradient distribution of trichomes generates a

macroscopic wettability gradient from the leaf tip to base, which drives liquid directional transport *via* the surface energy gradient. Remarkably, the trichomes' continuously varying morphology achieves rapid liquid propagation through reduced interwing spacing, creating an apparent wetting gradient that operates even on hydrophobic substrates.

Crassula muscosa shoots (Fig. 4f) exhibit a unique capability for selectively directional liquid transport through the asymmetric reentrant leaf geometry.[130] Variations in reentrant angles induce heterogeneous meniscus formation, where partial pinning at the lower fin edge in the negative direction enhanced the heterogeneity. As the advancing meniscus front reaches an adjacent fin, the capillary action at the corners accelerates liquid transfer across the fin, achieving velocities nearly 20 times faster than inter-fin propagation, while flow in other directions is suppressed. Upon crossing, a new meniscus forms and spreads directionally toward the next fin, establishing a self-sustaining cycle of selective liquid transport along the shoot surface.

Araucaria leaves have evolved ratchet structures with dual curvature that enable surface-tension-dependent liquid transport (Fig. 4g).[42] With periodic spines tilted toward the leaf tip, the unique geometry exhibits an opposite liquid manipulation direction. Specifically, low-surface-tension liquids (*e.g.*, ethanol) follow the ratchet inclination, while high-surface-tension liquids (*e.g.*, water) move oppositely. The mechanism of this bidirectional liquid manipulation is asymmetric contact line pinning induced by the reentrant curvatures.

These natural organisms demonstrate evolutionarily refined structural anisotropies that enable effective liquid control strategies. By synergistically integrating directional wettability gradients, unbalanced Laplace pressures, and capillary dynamics, biologically optimized architectures achieve remarkable liquid manipulation.

The universal biological strategies of surface wettability and asymmetric structures establish a powerful design platform. This platform, in turn, guides the development of engineering liquid manipulators capable of precisely controlling liquid behaviours to meet diverse application requirements.

4. On-demand control of liquid surface deformation by engineered manipulators

By learning from nature's wisdom in surface engineering, researchers have created advanced liquid manipulators that enable on-demand control of liquid transport or surface deformation across 1D, 2D, and 3D trajectories. The core control strategies of these manipulators rely on proper surface wettability and well-designed structures to direct liquid motion or regulate liquid surface shape. These manipulators transform fundamental physical principles into platforms that merge operational simplicity with control accuracy, designed to meet diverse application needs, from guiding microfluidic flows in lab-on-a-chip diagnostics to enhancing droplet transport in atmospheric water collectors and facilitating selective chemical separation in industrial settings.[131,132]

4.1. Liquid movement along 1D trajectories

Controllable liquid motion relies on applying unbalanced forces, orthogonally decomposable into three fundamental components: horizontal (Fig. 5a(i)), vertically upward (Fig. 5b(i)), and vertically downward (Fig. 5c(i)). Through the comprehensive investigation of liquid transport dynamics under these unbalanced forces, we could understand controllable liquid behaviour under arbitrary directional force effects. Gravity exhibits orientation-specific influences, becoming negligible in horizontal manipulation where it acts perpendicular to motion, resistive in upward vertical transport where it opposes the driving force, and assistive in downward vertical flow where it augments the applied force. This analytical approach reveals how solid manipulators, decorated with asymmetric microstructures, can generate the requisite forces to overcome or harness gravity, enabling precise control of the liquid morphology and transport pathways in engineered systems.

Fiber-like structures with asymmetric topography, exemplified by spider silk-inspired spindle knots and cactus spine-derived conical designs, enable efficient horizontal liquid transport. These systems efficiently harvest discrete airborne droplets in humid environments and direct them along predefined paths (Fig. 5a(ii)).[133] For instance, cavity-microfibers can absorb ambient moisture. Randomly condensed microdroplets subsequently grow *via* continuous vapor deposition and directionally migrate toward spindle knots due to the combined influence of surface energy gradients and Laplace pressure differences between knots and joints. This directional transport leads to progressive droplet coalescence at knots.

The system's maximum water collection capacity per single cavity-fiber is ultimately determined by the equilibrium between droplet adhesion and gravitational forces, with droplets detaching once exceeding the critical volume. Theoretical analysis yields the maximum sustainable droplet volume as (V):

$$V = \frac{\gamma \cos\theta L}{\rho g} \tag{12}$$

where L characterizes the length of the three-phase contact line at the liquid–solid–air interface, which is intrinsically determined by the spindle knot's geometric configuration. This relationship demonstrates that the volume of detaching droplets can be tuned by engineering the spindle knot's size parameters, particularly through modulation of its minor semi-axis and optimization of the liquid–solid contact length. Typical manufacturing methods of the microfibers with spindle-knots are electrospinning,[134,135] dip-coating,[136,137] and microfluidic approaches.[138]

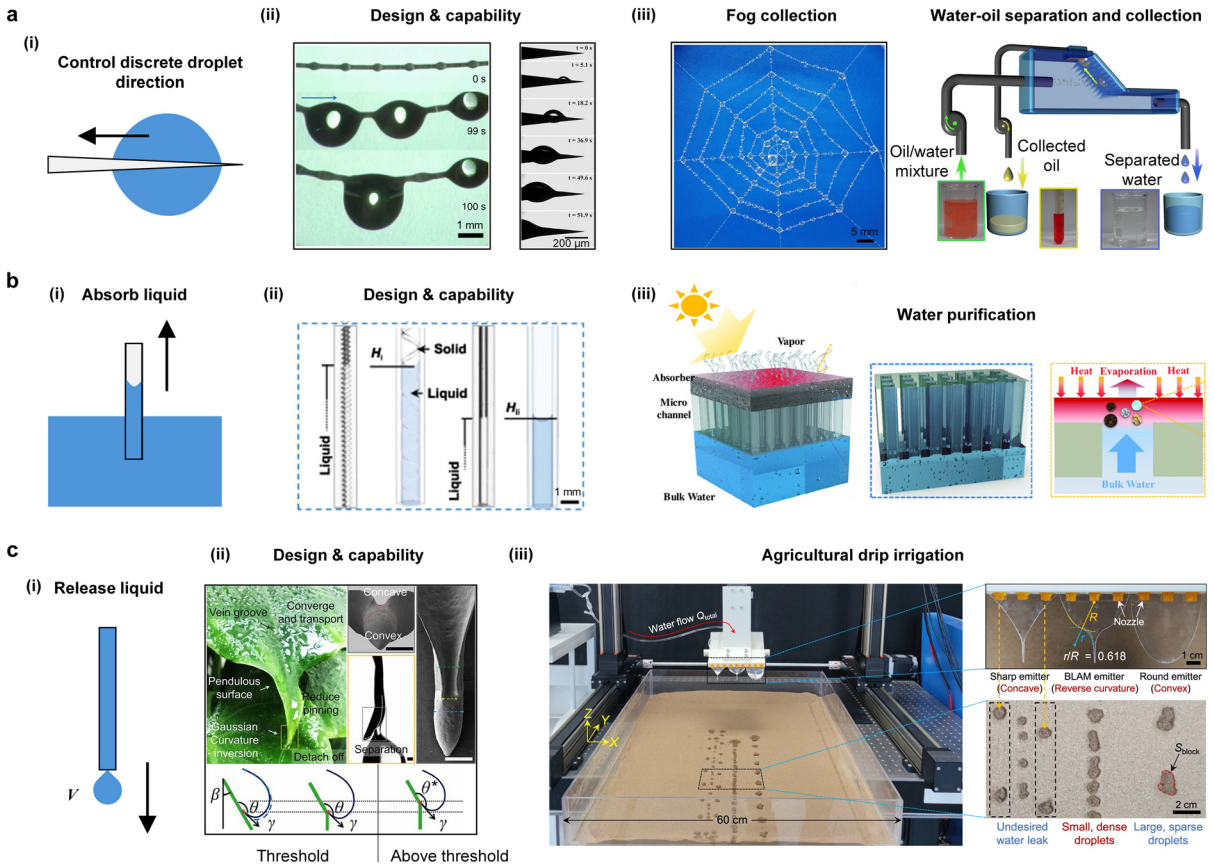

Fig. 5 Schematic, design, capability and applications of controllable 1D liquid movement along (a(i)–(iii)) horizontal, (b(i)–(iii)) vertical upward, and (c(i)–(iii)) vertical downward directions. The spider silk images of (a(ii)) and (a(iii)) are reprinted with permission from ref. 133. Copyright 2017, Springer Nature. The cone-tip structure image of (a(ii)) is reprinted with permission from ref. 139. Copyright 2013, Wiley. The oil–water separation figure of (a(iii)) is reprinted with permission from ref. 143. Copyright 2013, Springer Nature. The figure of (b(ii)) is reprinted with permission from ref. 146. Copyright 2025, Institute of Physics Publishing. The figure of (b(iii)) is reprinted with permission from ref. 148. Copyright 2022, Wiley. The figure of (c(ii)) is reprinted with permission from ref. 35. Copyright 2020, National Academy of Sciences. The figure of (c(iii)) is reprinted with permission from ref. 150. Copyright 2023, Springer Nature.

The cactus spine-inspired conical structure can be precisely engineered with tailored wettability, ranging from uniform hydrophobic/hydrophilic to spatially gradient patterns, to achieve directional liquid transport. Take water droplet movement on the hydrophilic surface as an example (Fig. 5a(ii)).[139] The water droplet grows on the tip of the conical structure and moves toward the base part. During this transport, the droplet undergoes a distinct morphological transition from a barrel to a clamshell configuration, which fundamentally alters droplet dynamics.[140] Common fabrication approaches like electrochemical corrosion and chemical modification enable wettability programming by creating micro/nanoscale features and functional group distributions.

As shown in Fig. 5a(iii), these fiber-like structures are ideal for sustainable fog harvesting applications, as an eco-friendly water recovery strategy.[141,142] Due to different wettability responses to distinct liquid, these solid structures can selectively control target liquids (*e.g.*, oil collection) while rejecting others (*e.g.*, water repulsion), thereby achieving highly efficient oil–water separation.[143–145]

Vertically upward liquid transport typically relies on narrow tubes with capillary effects, as shown in Fig. 5b(i). In nature, plants like young pumpkin stems and *Nepenthes alata* have evolved far more sophisticated microstructural solutions for liquid transport. Inspired by these biological designs, researchers have developed structure-decorated microchannels using 3D printing, such as helicoidally patterned[146] and peristome-mimetic structures,[147] achieving approximately twice the liquid lifting height of similarly sized smooth microchannels (Fig. 5b(ii)) due to the enhanced capillary effect. Take the helicoidal microstructures as an example. They promote additional meniscus formation, reducing the radius of curvature and significantly increasing capillary pressure. Additionally, the patterned microstructures provide partial fluid support, further improving microfluidic performance. This biomimetic approach demonstrates how nature-inspired designs can outperform conventional methods in capillary-driven liquid transport. A key application requiring vertical liquid transport is water purification, as illustrated in Fig. 5b(iii).[148] This system utilizes solar energy to purify

wastewater and seawater. Microchannels first absorb the contaminated water, then filter impurities through adsorption along their walls, and finally collect purified water vapor generated by solar evaporation.

The typical purpose of controlling liquid vertically downward is to control the falling volume of droplets from the solid surface (Fig. 5c(i)). In general, on a non-hysteretic substrate, a droplet can only detach and fall when gravity (F_G) overcomes the surface's adhesive forces, *i.e.*, a balance governed by both gravitational pull and liquid–solid adhesion. For instance, on an inclined surface with tilt angle β (Fig. 5c(ii)), the primary adhesive force stems from capillary effects (F_C), and droplet detachment occurs when:[149]

$$F_G = \rho g V \cos\beta > F_C = \gamma W \cos\theta \quad (13)$$

where V indicates the droplet volume and W corresponds to the contact width between the droplet and the surface front. There exist critical depinning conditions when F_G equals F_C, and the threshold values of droplet volume (V_C) and contact width (W_C) satisfy the following relationship:

$$W_C/V_C \sim \rho g \cos\beta/|\gamma \cos\theta| \quad (14)$$

Consequently, a steeply inclined leaf surface (small β) enhances the gravitational component, reducing V_C. When β is fixed, the bending position along the inclined surface further influences V_C. As illustrated in Fig. 5c(ii), threshold droplets maintain a stable triple contact line (TCL) at a specific contact width W on a flat incline. If the surface bends precisely at the threshold contact line, the droplet remains stable. In contrast, bending the surface above the TCL disrupts equilibrium, increasing the gravitational force component while reducing capillary resistance, thus triggering droplet instability. This force redistribution causes the droplet to detach at a smaller volume than would be required on a uniformly inclined surface. The decreased volume of falling droplets allows effective agricultural drip irrigation (Fig. 5c(iii)), benefiting water saving, fast sprouting, and upright growth of crop seedlings. When the irrigation surface is placed vertically ($\beta = 0$), the falling droplet volume is smallest unless further optimization, such as surface front curvature[150] and microstructure decoration of surface.[151]

As the manipulated liquid volume is further reduced (such as microliters or even nanoliters), gravity, which is a kind of body force, has little effect on such small-volume droplets. Therefore, to achieve controllable droplet release, it is necessary to introduce a stronger force to resist adhesion, such as mechanical force.[152] In addition, combining the upward and downward forces to control the liquid can achieve liquid transfer.[153]

These capabilities in unidirectional liquid control represent a major step forward in fluid manipulation technology, with far-reaching implications for applications requiring directed liquid transport from the source to the target,[154] such as precision agriculture, water source collection and industrial water processing. Harnessing these fundamental control mechanisms enables breakthrough liquid management capabilities, paving the way for more efficient, accurate, and sustainable liquid resource utilization across science and engineering.

4.2. Liquid transport/patterning on 2D planes

Applying forces to liquids within a 2D plane can be categorized into two distinct scenarios. The first involves sequential application of forces along multiple directions, enabling liquid transport along complex trajectories. The second scenario employs simultaneous application of forces along multiple directions to spatially confine liquids into predetermined shapes or restricted areas, with extreme confinement (as seen on superhydrophobic surfaces) producing quasi-spherical droplet formations. This dimensional expansion of fluid control fundamentally transforms liquid handling paradigms. While 1D manipulation remains essential for basic directional transport and many practical applications, 2D control unlocks significantly more advanced capabilities, such as innovative microfluidic technologies and anti-fouling superhydrophobic surfaces. The ability to precisely control both the position and morphology of liquids in 2D space represents a major breakthrough in microfluidics, enabling sophisticated liquid-based systems that integrate engineering functionality at unprecedented scales.

As illustrated in Fig. 6a(i), pre-designed asymmetric surface structures enable precise control of complex liquid transport trajectories. For example, a flat superhydrophilic surface integrated with 2D barriers, which induce anisotropic resistance, controls liquid transport along the preferential direction (Fig. 6a(ii)).[155] These barriers provide a simple yet robust solution for long-range liquid manipulation on open surfaces. Through adjusting the tilt angle, the transport direction can be regulated, and steeper angles reduce spreading resistance, allowing sequential directional control. Controllable liquid transport in 2D planes has important applications in biochemical analysis and high-throughput drug screening in both air and liquid environments,[156–160] where samples can be precisely positioned and retrieved at any point within the microfluidic network. A notable implementation is the open microfluidic chip shown in Fig. 6a(iii), which enables autonomous liquid absorption, propulsion, and complete mixing.[161] When the manipulated fluid is a functional liquid such as a coolant, its performance can be significantly enhanced on surfaces engineered with specific asymmetric structures, enabling applications like highly efficient steel pipe cooling.[162] More innovatively, liquid transport trajectories can be the medium for information transmission.[163] For example, the surface is designed only to permit directional transport for liquids with specific liquid–solid interfacial energy relationships (quantified by the ratio $\zeta = \gamma_S/\gamma_L$, where γ_S is the surface free energy and γ_L is the liquid surface tension) (Fig. 6a(iv)).[164]

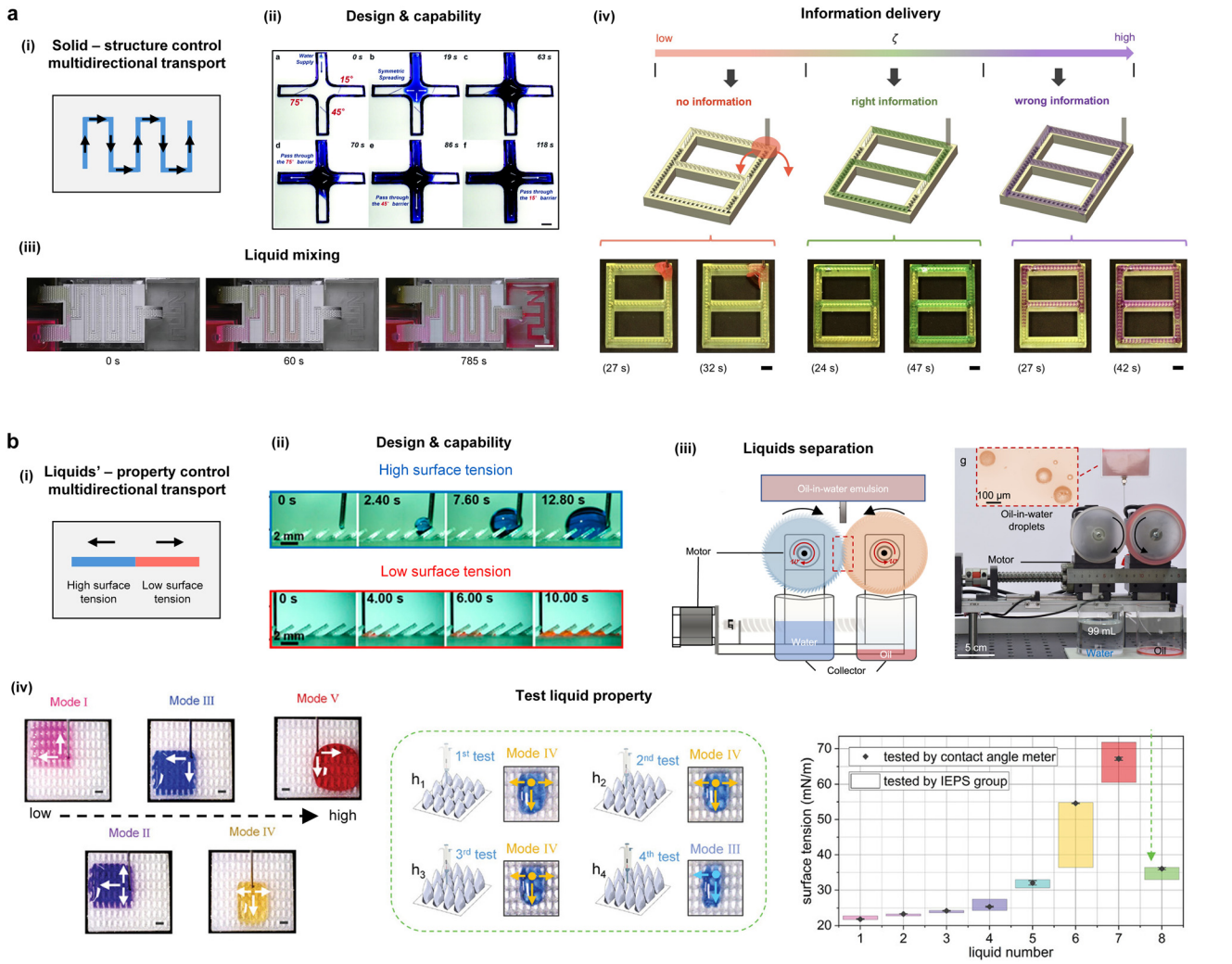

Fig. 6 Schematic, design, capability and applications of multi-directional liquid transport. (a(i)–(iv)) The structure of the solid surface induced complex 2D liquid spreading trajectories. (b(i)–(iv)) The liquid intrinsic properties determined specific spreading directions. The figure of (a(ii)) is reprinted with permission from ref. 155. Copyright 2014, The Royal Society of Chemistry. The figure of (a(iii)) is reprinted with permission from ref. 161. Copyright 2023, Wiley. The figure of (a(iv)) is reprinted with permission from ref. 164. Copyright 2025, American Chemical Society. The figure of (b(ii)) is reprinted with permission from ref. 165. Copyright 2018, American Chemical Society. The figure of (b(iii)) is reprinted with permission from ref. 166. Copyright 2023, Springer Nature. The figure of (b(iv)) is reprinted with permission from ref. 168. Copyright 2024, Wiley.

This forms the basis for a novel liquid-based encryption system, where information is encoded in surface patterns and is only decipherable using liquids with precise ζ values acting as decryption keys. The system demonstrates three distinct regimes: at low ζ values, liquids accumulate near injection points without revealing information; at high ζ values, uncontrolled bidirectional transport displays incorrect information; only within the appropriate ζ range does the liquid properly convey the intended message, creating a sophisticated platform for secure information transfer through controlled fluid dynamics.

Direction-specific manipulation tailored to liquid properties enables advanced functionalities (Fig. 6b(i)), which is typically achieved through submillimeter to millimeter-scale asymmetric structures fabricated *via* 3D printing, leveraging Laplace pressure differences to directionally transport different liquids. For instance, ethanol (low surface tension) flows right while water (high surface tension) moves left (Fig. 6b(ii)).[165] Such property-specific directional control has critical application in liquid separation systems, exemplified by the gear system that effectively separates oil–water emulsions (Fig. 6b(iii)).[166] This system combines surface superwettability with complementary topological structures to achieve continuous separation: water and oil rapidly form distinct, mutually repelling films on their respective preferential gear surfaces, while the gears' rotational motion and overflow design maintain high separation flux by preventing fouling-induced performance degradation, which is an important improvement over oil–water separators based on 1D droplet moving trajectories. Moreover, this principle enables innovative liquid characterization methods.[167] As shown in Fig. 6b(iv), surfaces

are decorated with structured units, which have bottom-up multi-curvature features, thus directing liquids of different surface tensions into five distinct spreading modes under Laplace pressure gradients.[168] By fabricating surfaces with progressively increasing unit heights ($h_1 < h_2 < h_3 < h_4$), they offer a portable surface tension indicator that refines measurement accuracy through mode-based classification. More significantly, this technology holds transformative potential as a versatile characterization tool capable of quantifying any physicochemical parameter that influences liquid surface tension, including solvent composition changes, temperature effects, or the presence of surface-active contaminants. The approach establishes a generalized paradigm for liquid property analysis through interfacial behaviour observation.

Multi-directional control of liquid transport trajectories further extends to thermal management applications through phase-change-enhanced heat dissipation, where controlled liquid generates vapor phases with high surface-to-volume ratios and latent heat benefits.[169] A notable implementation is a thermal regulator combining Tesla valves with engineered capillary structures to rectify chaotic two-phase flow into directional transport, significantly boosting heat transfer coefficients and critical heat flux in its activated state.[170] Conversely, thermal fields can also actively drive liquid motion through mechanisms such as the Leidenfrost effect, where localized vaporization creates self-propulsion of droplets, demonstrating another dimension of thermo-fluidic coupling.[171,172]

Besides the aforementioned control of the fluid transport direction through the design and fabrication of specific structures on fully open surfaces, the geometric shaping of surface channels, including their parameters and internal structural features, enables further regulation of additional liquid properties, such as flow resistance. Specifically, the design of channels with specialized shapes (*e.g.*, spiral forms[173]) or the incorporation of asymmetric structures embedded within channels can modulate liquid behaviour, such as vortex dynamics and flow velocity.[174,175] Such control is essential for high-efficiency particle separation, including polymer particles and cells, and holds significant value for both laboratory and commercial development of microfluidic systems in life and materials sciences.[176–178]

In practical applications of channel-based microfluidic systems, the intrusion of gas into water-filled microchannels often complicates liquid transport dynamics. This phenomenon can lead to gas blockages that severely disrupt continuous flow within microfluidic chips. Therefore, it is essential to design channel geometries and dimensional parameters that facilitate thorough investigation of gas-induced flow obstruction dynamics.[179] Such a fundamental understanding is critical for developing stable and robust microfluidic devices.

Simultaneous application of forces along multiple directions to liquids enables precise spatial confinement of liquid surfaces, as demonstrated in Fig. 7a(i), where the droplet stabilized between four pillars forms well-defined liquid–environment interfaces, creating functional modular units capable of independent operation or programmed assembly. Such a liquid confinement strategy allows the construction of reconfigurable liquid devices with complex geometries and precisely controlled liquid–liquid interfaces (Fig. 7a(ii)),[180] achieved through a 3D-printed pillar array substrate, immersed in silicone oil that facilitates *in situ* liquid unit formation *via* surface tension effects. The system exhibits distinct assembly behaviours where miscible liquids spontaneously merge into homogeneous structures while immiscible liquids maintain predetermined interfacial configurations. The underlying mechanism of maintaining the liquid unit arises from the resistance caused by Laplace

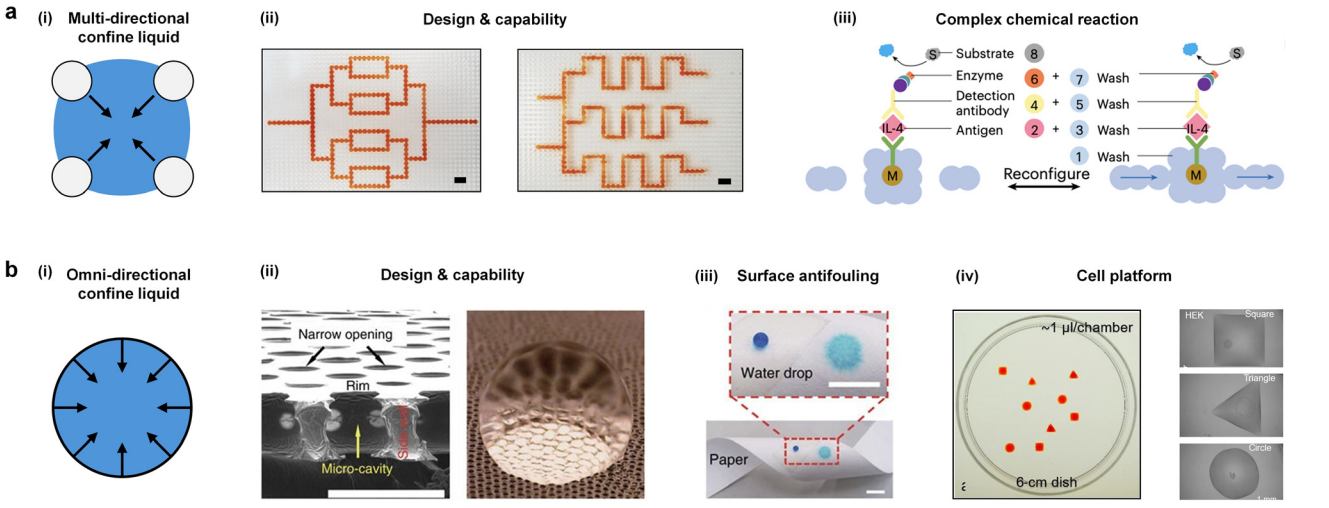

Fig. 7 Schematic, design, capability and applications of liquid surface shape manipulation by liquid–solid interactions. (a(i)–(iii)) Multi-directional confinement applied on a liquid unit. (b(i)–(iv)) Omni-directional confinement of small liquid volumes. Figures of (a(ii)) and (a(iii)) are reprinted with permission from ref. 180. Copyright 2024, Springer Nature. Figures of (b(ii)) and (b(iii)) are reprinted with permission from ref. 181. Copyright 2017, Springer Nature. The figure of (b(iv)) is reprinted with permission from ref. 182. Copyright 2019, The American Association for the Advancement of Science.

pressure from convex water–oil interfaces, preventing liquid spreading, and thus creating mechanically stable liquid modules. The reconfigurable characteristic of such liquid units enables rapid connection, separation, and modification of liquid architectures, dramatically simplifying complex experimental workflows by integrating multiple processing steps, including alternating reaction and washing steps, into a single device. Fig. 7a(iii) shows the successful execution of all eight steps in human IL-4 protein ELISA using liquid unit constructed microfluidic channels. The system's dynamic reconfigurability provides unique advantages. When channels are disconnected, isolated microreactors form for specific reaction steps (2, 4, 6, and 8), preventing reagent waste in flow paths and connected equipment; when reconnected, integrated channels enable efficient washing steps (1, 3, 5, and 7) *via* simple syringe pump operation. Notably, the open architecture of this chip design permits sampling from any region at any processing stage without bubble disturbance, which is a critical advantage unachievable in conventional microfluidic systems. This innovative approach establishes a new paradigm for modular liquid manipulation that combines the precision of microfluidics with the flexibility of macroscopic fluid handling.

The extreme case of multi-directional liquid manipulation involves applying forces along omni-directions to liquids within a 2D plane, as demonstrated in Fig. 7b(i). This is typically achieved through liquid-repellent surfaces that exert uniform forces in all directions, causing the liquid–solid contact area to form a circular interface while the droplet itself assumes a near-spherical shape. A breakthrough example shown in Fig. 7b(ii)[181] presents a durable omniphobic membrane fabricated *via* microfluidic emulsion templating, featuring interconnected honeycomb microstructures with precisely engineered re-entrant geometries that provide exceptional liquid repellency. The membrane's flexible polyvinyl alcohol (PVA) composition allows for conformal coating on diverse substrates, including glass tubes and paper, as illustrated in Fig. 7b(iii). Besides solid surfaces, an alternative approach utilizes immiscible liquid–liquid interfaces to achieve omnidirectional confinement. Fig. 7b(iv) demonstrates how standard cell culture dishes can be transformed into reconfigurable microfluidic platforms by strategically manipulating liquid–liquid interfaces around adherent cells.[182] This innovative technique, employing immiscible liquids as structural elements, enables critical biological applications including single-cell cloning, selective cell isolation, drug screening, and wound healing studies. The method's biological compatibility and operational simplicity address longstanding barriers to microfluidic adoption in life sciences,[183,184] potentially accelerating the translation of microfluidic technologies from engineering prototypes to mainstream biological research tools that finally realize their transformative potential in biomedical applications.

In certain applications, control of liquid multidirectional transport and confinement of liquid surface shape have demonstrated exceptional performance. For example, anisotropic microstructured surfaces enable directional liquid sheeting, effectively removing low-surface-tension contaminants and small particles.[185,186] 2D liquid control systems outperform their 1D counterparts in droplet collection, demonstrating accelerated droplet growth rates, faster nucleation onset, higher steady-state turnover efficiency, and greater total collected volumes. This enhancement is achieved through optimized structural designs, including convex features that improve vapor diffusion flux, widening slope structures that promote downward droplet transport before the growth rate decline, and specialized nano coatings that facilitate synergistic interactions between coalescence-driven growth and capillary-assisted motion.[187] Additionally, precise control over the three-phase contact line (TCL) retreat allows the fabrication of complex 3D structures from a single resin droplet.[188] Moreover, retaining specific liquids within surface microstructures enables the transport of immiscible droplets,[189] drag reduction,[190] and friction noise suppression.[191] These applications highlight the advantages of multi-directional liquid manipulation in 2D space: by simultaneously regulating interfacial forces along multiple directions, it enables complex fluid behaviours, opening new possibilities in surface engineering, microfluidics, and functional material design.

4.3. Programmable liquid manipulation in 3D space

3D liquid manipulation can be categorized into two primary approaches: controlling the 3D flow trajectories of liquids and programming the liquid surface morphology within 3D space. These strategies not only enable more sophisticated liquid control but also allow the creation of unprecedented complex liquid interfaces with tailored functionalities. Remarkably, besides maintaining the ability to handle liquids as conveniently as solids (permitting precise pickup, transportation, and deposition), the 3D programming of liquid surfaces maximizes the interfacial contact area between the liquid and its environment. This enhanced interface facilitates optimal mass and energy exchange, making the technology particularly valuable for applications in advanced microfluidics, biochemical reactors, and smart manufacturing systems where precise liquid control and efficient interfacial interactions are critical.

A highly effective strategy for achieving 3D liquid transport trajectories is fabricating flexible liquid manipulators (Fig. 8a(i)). This approach enables on-demand adjustment of liquid pathways through material deformation. A prime example is the flexible liquid diode microtube fabricated *via* pulsed microfluidics, which achieves directional liquid transport through asymmetric pinning effects and unbalanced Laplace pressure.[192,193] The microtube's pliable nature allows versatile configurations. Specifically, it can be coiled around cylindrical structures, freely suspended, or placed in surface-contact arrangements (Fig. 8a(ii)). Such flexible 3D liquid

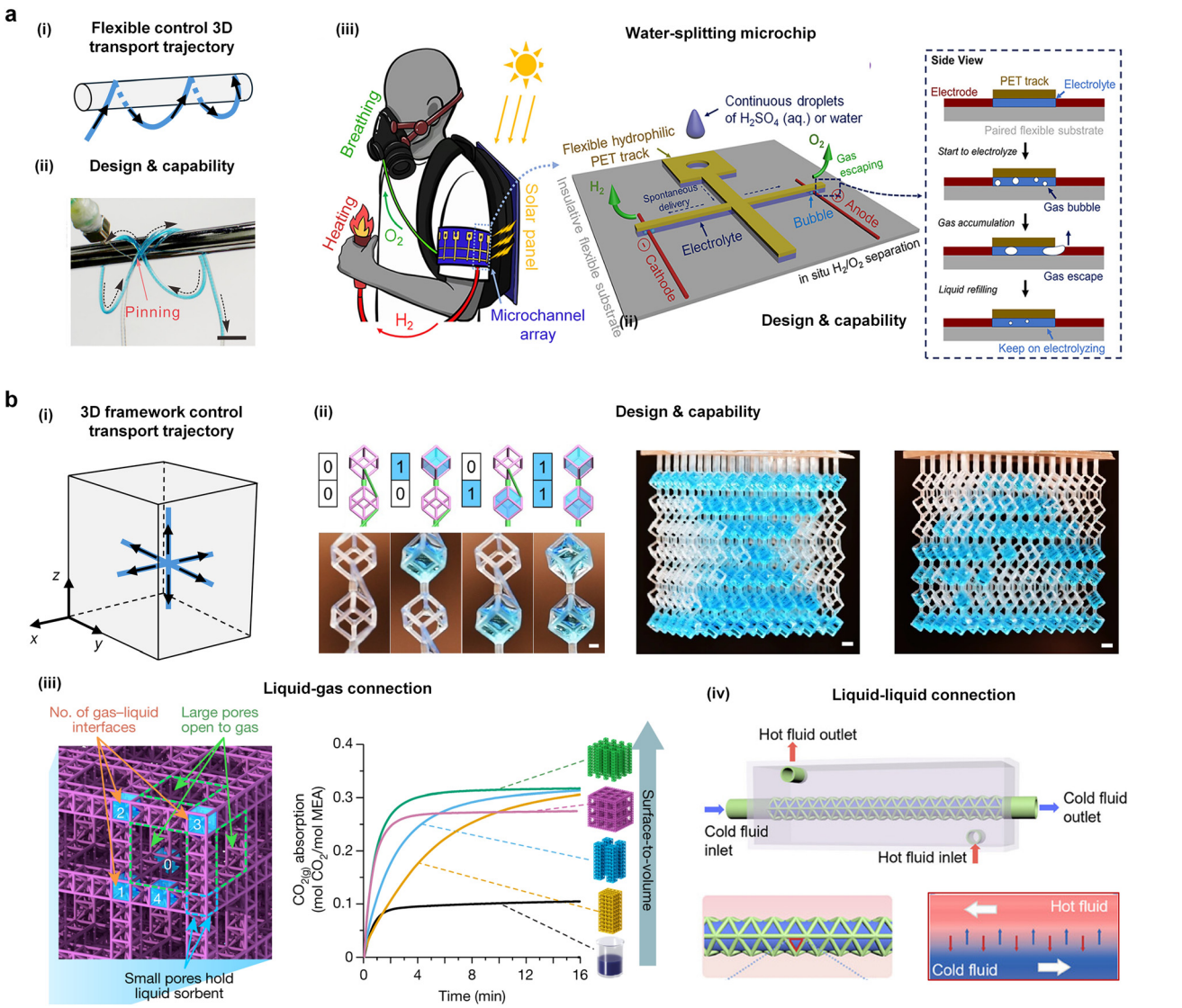

Fig. 8 Schematic, design, capability and applications of controllable 3D complex liquid behaviours. (a(i)–(iii)) Soft liquid manipulators guided 3D flexible spreading trajectories. (b(i)–(iv)) The 3D liquid manipulation framework governed programmable liquid–environment interfaces. The figure of (a(ii)) is reprinted with permission from ref. 192. Copyright 2024, National Academy of Sciences. The figure of (a(iii)) is reprinted with permission from ref. 195. Copyright 2024, Elsevier. The figure of (b(ii)) is reprinted with permission from ref. 196. Copyright 2024, Springer Nature. The figure of (b(iii)) is reprinted with permission from ref. 197. Copyright 2021, Springer Nature. The figure of (b(iv)) is reprinted with permission from ref. 198. Copyright 2025, Wiley.

manipulators are particularly valuable for portable and wearable fluidic devices.[194] For example, they can be integrated into electrolysis systems to create compact and wearable water-splitting microchips. A practical implementation could involve using in cold, polluted regions, where solar-powered hydrogen production provides heating fuel while simultaneously generating breathable oxygen (Fig. 8a(iii)).[195] The ability to control flexible 3D liquid trajectories enables adaptive liquid manipulation in constrained space, which is crucial for portable energy systems and wearable medical devices.

Programming the 3D liquid surface morphology through solid frameworks enables omnidirectional liquid manipulation within 3D space (Fig. 8b(i)), where controlled liquid capture and release are achieved through capillary effects and drainage channels formed by liquid films. The underlying mechanism involves single-rod-connected frames that function as liquid capture units, while double-rod-connected frames create interconnecting liquid films that bridge the framed liquid with the bulk reservoir below, enabling programmable release, constructing a system capable of generating complex 3D liquid patterns (Fig. 8b(ii)).[196] This solid-framework-based liquid programming technique significantly enhances liquid–environment interactions by creating optimized interfacial architectures. In gas absorption applications (Fig. 8b(iii)), the engineered frameworks dramatically increase liquid–gas contact areas, substantially improving processes like CO_2 capture through enhanced transport of gaseous molecules into liquid sorbents.[197] Similarly, for

thermal management (Fig. 8b(iv)), these frameworks provide unprecedented control over continuous flow while maintaining open interfaces, eliminating the heat transfer limitations imposed by conventional pipe walls and enabling the development of highly efficient wall-less heat exchangers.[198] The ability to program complex 3D liquid surfaces using solid frameworks represents a paradigm shift in fluid manipulation, as it combines the precision of engineered structures with the dynamic adaptability of liquids, enabling tailored interfacial geometries that optimize mass and energy transfer processes while maintaining the fundamental transport advantages of liquid systems. This approach opens new possibilities in chemical processing, energy systems, and thermal management, where enclosed fluid handling systems face fundamental limitations.

Extending the concept of manipulating liquids within 3D space to surfactant-mediated systems introduces a dynamic temporal dimension to spatial control. For example, surfactant solutions can autonomously navigate complex 2D mazes through exogenous–endogenous surfactant interactions.[199,200] The incorporation of surfactants creates responsive liquid–solid interfaces where Marangoni stresses can be programmed to evolve spatially and temporally, enabling autonomous reconfiguration of liquid morphologies within predefined trajectories. This synergistic combination allows solid matrices to define static morphological boundaries while surfactant gradients dictate dynamic flow pathways, achieving coordinated liquid manipulation.

The engineered systems can be artificially designed to meet precise application requirements. This is achieved by recognizing fluidic processes as specific dimensional tasks, controlling liquid motion along 1D paths, across 2D surfaces, or within 3D spaces. By focusing on the specific behavioural requirements of liquids in a targeted dimension, researchers can develop specialized manipulators that apply the most appropriate control mechanisms, whether through tailored surface wettability, and optimized geometric features. This engineering approaches offer superior flexibility and tailorability for liquid manipulation, extending capabilities beyond what is commonly observed in the natural world.

5. Conclusions and outlook

Fluidity provides unparalleled advantages for energy and mass transfer,[201] enabling liquids as indispensable media for diverse applications that demand tuneable physical properties or matter exchange, such as thermal management,[202] soft robotics,[203,204] biomolecular analysis,[205,206] chemical reactions,[207] and functional material synthesis.[208,209] A challenge is that no single liquid manipulator can optimally serve all these distinct applications due to their divergent requirements. Instead, the solution lies in application-specific design, where liquid manipulators are tailored by considering the primary liquid morphology and its interaction dynamics with surrounding phases in each application. This targeted approach enables on-demand liquid control, with liquid macro behaviours categorized as controlled motion in 1D trajectories, 2D planes, and 3D space. By constructing dimension-specific (1D, 2D, or 3D) liquid manipulators designed with asymmetric structures, we can achieve efficient liquid control through simplified architectures and enhanced liquid utilization efficiency, mirroring nature's elegant, energy-minimizing strategies observed in biological systems.

Each liquid manipulation strategy in different dimensions is suitable for specific liquid–solid–gas interaction. 1D trajectory-based liquid manipulation excels in targeted liquid collection from the source to destination (Fig. 9a). Typical scenarios include directional transport of gaseous-phase liquids on solid surfaces through designed wettability gradients and micro/nanostructures, and selective extraction and drainage of discrete liquid volumes from bulk liquids or immiscible mixtures *via* surface-mediated adsorption/expulsion mechanisms. These 1D liquid manipulators overcome intrinsic liquid mobility challenges, enabling rapid liquid movement, though they face practical constraints including volume limitations and long-term efficacy issues such as drainage delays or residual contamination. Arranging 1D asymmetric structures into 2D arrays unlocks complex planar liquid control (Fig. 9b). This approach enables thorough liquid–liquid mixing and reactions, and liquid–solid energy/matter transfer (exemplified by surface cooling and contaminant removal) *via* long-range and intricate transport pathways, and liquid morphology confinement. Current 2D surfaces, however, remain constrained to single predefined trajectories for one kind of liquid, necessitating complete device redesign for pathway modification, which is a significant barrier to flexible implementation.

3D structural manipulation achieves programmable liquid morphologies with partial liquid–solid contact and direct liquid–environment interaction (Fig. 9c), offering distinct advantages. Maximized specific surface area enhances gas absorption and release, and direct interfacial contact accelerates reaction kinetics, which is integrable with conventional systems (*e.g.*, heat exchangers) and enables novel performance. However, like 1D liquid manipulators, these architectures remain susceptible to liquid retention on high-energy solid surfaces, limiting operational reusability.

Future progress demands deeper investigation of dynamic interphase phenomena. Engineering precursor film propagation could harness liquid–liquid interaction forces to achieve ultrafast transport beyond current limits. Integrating post-wetting behaviours, such as meniscus oscillation and coalescence dynamics, into structural designs may resolve drainage constraints. Furthermore, 3D nanoconfinement architectures show promise for stabilizing liquid films on surfaces, potentially overcoming depletion issues in slip surfaces. These frontiers underscore the field's development toward precisely orchestrated multiphase interactions across scales.

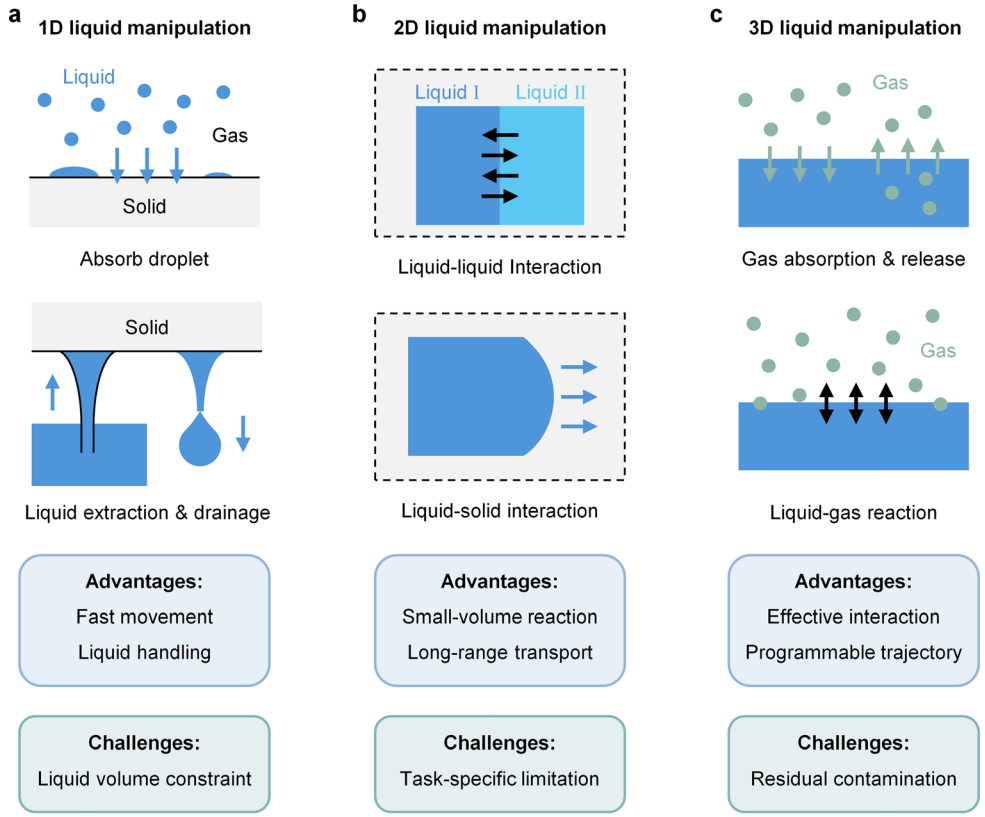

Fig. 9 Summary of (a) 1D, (b) 2D, and (c) 3D liquid manipulation strategies, including the suitable liquid morphologies for each strategy and their interactions with surrounding phases, as well as respective advantages and disadvantages.

Author contributions

Siqi Sun: investigation, writing – original draft, writing – review & editing. Liqiu Wang: supervision, funding acquisition, writing – review & editing. Yiyuan Zhang: supervision, funding acquisition, investigation, writing – review & editing.

Conflicts of interest

There are no conflicts to declare.

Data availability

No primary research results, software or code have been included, and no new data were generated or analysed as part of this review.

Acknowledgements

The financial support from the Research Grants Council of Hong Kong (GRF 15309825, 17213823, and 17205421) and the Hong Kong Polytechnic University (SHS Chair Professor: P0045687; SHS Assistant Professor: P0058250 and P0048083) is acknowledged.

Notes and references

1 C. W. Lo, Y. C. Chu, M. H. Yen and M. C. Lu, *Joule*, 2019, **3**, 2806–2823.
2 L. Mohapatra and S. H. Yoo, *Chem. Eng. J.*, 2024, **481**, 148537.
3 B. Wang, X. Luo, Y. Feng, L. Yang, C. Zhang, Z. Dong, L. Jiang and H. Dai, *Adv. Sci.*, 2022, **9**, 2204244.
4 Q. Wang, X. Yao, H. Liu, D. Quéré and L. Jiang, *Proc. Natl. Acad. Sci. U. S. A.*, 2015, **112**, 9247–9252.
5 M. Prakash, D. Quéré and J. W. M. Bush, *Science*, 2008, **320**, 931–934.
6 H. F. Bohn and W. Federle, *Proc. Natl. Acad. Sci. U. S. A.*, 2004, **101**, 14138–14143.
7 C. Zhang, S. Guo, X. Liu, Z. Guo, C. Yu, Y. Ning, K. Liu and L. Jiang, *Appl. Phys. Rev.*, 2024, **11**, 021316.
8 W. Li, Z. Wang, F. Yang, T. Alam, M. Jiang, X. Qu, F. Kong, A. S. Khan, M. Liu, M. Alwazzan, Y. Tong and C. Li, *Adv. Mater.*, 2019, **32**, 1905117.
9 C. Zhang, M. Cao, H. Ma, C. Yu, K. Li, C. Yu and L. Jiang, *Adv. Funct. Mater.*, 2017, **27**, 1702020.
10 R. Wen, Q. Li, W. Wang, B. Latour, C. H. Li, C. Li, Y. C. Lee and R. Yang, *Nano Energy*, 2017, **38**, 59–65.
11 M. A. Shannon, P. W. Bohn, M. Elimelech, J. G. Georgiadis, B. J. Mariñas and A. M. Mayes, *Nature*, 2008, **452**, 301–310.
12 J. Miao, T. Zhang, G. Li, W. Shang and Y. Shen, *Adv. Eng. Mater.*, 2022, **24**, 2101399.

13 I. J. Wright, *et al.*, *Science*, 2017, **357**, 917–921.
14 H. Dai, Z. Dong and L. Jiang, *Sci. Adv.*, 2020, **6**, eabb5528.
15 M. Zhang, Z. Zheng, Y. Zhu, Z. Zhu, T. Si and R. X. Xu, *Chem. Eng. J.*, 2022, **433**, 134495.
16 H. Yue, Q. Zeng, J. Huang, Z. Guo and W. Liu, *Adv. Colloid Interface Sci.*, 2022, **300**, 102583.
17 S. R. Begum and A. Chandrasekhar, *iScience*, 2024, **27**, 108878.
18 H. V. Moradi and J. M. Floryan, *Procedia IUTAM*, 2015, **14**, 147–151.
19 P. Motta, M. L. Habegger, A. Lang, R. Hueter and J. Davis, *J. Morphol.*, 2012, **273**, 1096–1110.
20 A. K. Geim, S. V. Dubonos, I. V. Grigorieva, K. S. Novoselov, A. A. Zhukov and S. Y. Shapoval, *Nat. Mater.*, 2003, **2**, 461–463.
21 H. Lee, B. P. Lee and P. B. Messersmith, *Nature*, 2007, **448**, 338–341.
22 J. Ju, Y. Zheng and L. Jiang, *Acc. Chem. Res.*, 2014, **47**, 2342–2352.
23 C. Zhang, S. Guo, X. Liu, Z. Guo, C. Yu, Y. Ning, K. Liu and L. Jiang, *Appl. Phys. Rev.*, 2024, **11**, 021316.
24 C. Zhang, L. Wang, C. R. Crick and Y. Lu, *Prog. Mater. Sci.*, 2025, **147**, 101358.
25 J. Li, J. Li, J. Sun, S. Feng and Z. Wang, *Adv. Mater.*, 2019, **31**, 1806501.
26 H. Chen, T. Ran, Y. Gan, J. Zhou, Y. Zhang, L. Zhang, D. Zhang and L. Jiang, *Nat. Mater.*, 2018, **17**, 935–942.
27 J. Ju, H. Bai, Y. Zheng, T. Zhao, R. Fang and L. Jiang, *Nat. Commun.*, 2012, **3**, 1247.
28 S. Feng, J. Delannoy, A. Malod, H. Zheng, D. Quéré and Z. Wang, *Sci. Adv.*, 2020, **6**, eabb4540.
29 H. Yang, J. Wu and S. Yan, *Appl. Phys. Lett.*, 2014, **104**, 263701.
30 A. Lechantre, *et al.*, *Proc. Natl. Acad. Sci. U. S. A.*, 2021, **118**, e2025513118.
31 C. J. Harper, S. M. Swartz and E. L. Brainerd, *Proc. Natl. Acad. Sci. U. S. A.*, 2013, **110**, 8852–8857.
32 Y. Winter and O. V. Helversen, *J. Mammal.*, 2003, **84**, 886–896.
33 Y. Zheng, X. Gao and L. Jiang, *Soft Matter*, 2007, **3**, 178–182.
34 E. Siefert, *et al.*, *Nat. Commun.*, 2025, **16**, 4913.
35 T. Wang, Y. Si, H. Dai, C. Li, C. Gao, Z. Dong and L. Jiang, *Proc. Natl. Acad. Sci. U. S. A.*, 2020, **117**, 1890–1894.
36 Q. Wang, Y. He, X. Geng, Y. Hou and Y. Zheng, *ACS Appl. Mater. Interfaces*, 2021, **13**, 48292–48300.
37 H. Dong, N. Wang, L. Wang, H. Bai, J. Wu, Y. Zheng, Y. Zhao and L. Jiang, *ChemPhysChem*, 2012, **13**, 1153–1156.
38 B. Wang, H. Dai, C. Zhang, Z. Dong, K. Li and L. Jiang, *Adv. Mater. Interfaces*, 2022, **9**, 2102311.
39 K. Dutta and S. De, *J. Mater. Chem. A*, 2017, **5**, 22095–22112.
40 B. Bhushan, *Philos. Trans. R. Soc., A*, 2009, **367**, 1445–1486.
41 T. Shen, N. Li, S. Liu, C. Yu, C. Zhang, K. Yang, X. Li, R. Fang, L. Jiang and Z. Dong, *Int. J. Extreme Manuf.*, 2024, **6**, 035502.
42 S. Feng, P. Zhu, H. Zheng, H. Zhan, C. Chen, J. Li, L. Wang, X. Yao, Y. Liu and Z. Wang, *Science*, 2021, **373**, 1344–1348.
43 L. Yang, W. Li, J. Lian, H. Zhu, Q. Deng, Y. Zhang, J. Li, X. Yin and L. Wang, *Science*, 2024, **384**, 1344–1349.
44 W. Barthlott and C. Neinhuis, *Planta*, 1997, **202**, 1–8.
45 J. Lian, W. Li, L. Yang, H. Li, Q. Deng, H. Zhu, Y. Zhang, N. X. Fang and L. Wang, *Proc. Natl. Acad. Sci. U. S. A.*, 2025, **122**, e2421589122.
46 T. D. Wheeler and A. D. Stroock, *Nature*, 2008, **455**, 208–212.
47 M. Filippi, T. Buchner, O. Yasa, S. Weirich and R. K. Katzschmann, *Adv. Mater.*, 2022, **34**, 2108427.
48 R. Zilionis, J. Nainys, A. Veres, V. Savova, D. Zemmour, A. M. Klein and L. Mazutis, *Nat. Protoc.*, 2017, **12**, 44–73.
49 S. Xu, *et al.*, *Science*, 2014, **344**, 70–74.
50 F. Bian, L. Sun, L. Cai, Y. Wang, Y. Wang and Y. Zhao, *Small*, 2020, **16**, 1903931.
51 Y. Zheng, Y. Shao and J. Fu, *Nat. Protoc.*, 2020, **16**, 309–326.
52 N. J. Cira, A. Benusiglio and M. Prakash, *Nature*, 2015, **519**, 446–450.
53 M. Jiang, *et al.*, *Nature*, 2022, **601**, 568–572.
54 Z. Liu, Y. Si, C. Yu, L. Jiang and Z. Dong, *Chem. Soc. Rev.*, 2024, **53**, 10012–10043.
55 S. Zhou, L. Jiang and Z. Dong, *Chem. Rev.*, 2023, **123**, 2276–2310.
56 L. Hou, *et al.*, *Innovation*, 2023, **4**, 100508.
57 J. Xu, S. Xiu, Z. Lian, H. Yu and J. Cao, *Droplet*, 2022, **1**, 11–37.
58 M. Li, C. Li, B. R. K. Blackman and S. Eduardo, *Int. Mater. Rev.*, 2021, **67**, 658–681.
59 H. Bai, T. Zhao and M. Cao, *Chem. Soc. Rev.*, 2025, **54**, 1733–1784.
60 C. Li, B. Kim, J. Yoon, S. Sett and J. Oh, *Adv. Funct. Mater.*, 2023, **34**, 2308265.
61 J. Li, N. S. Ha, T. Liu, R. M. Dam and C. J. Kim, *Nature*, 2019, **572**, 507–510.
62 M. G. Pollack, A. D. Shenderov and R. B. Fair, *Lab Chip*, 2002, **2**, 96–101.
63 W. Wang, H. Vahabi, A. Taassob, S. Pillai and A. K. Kota, *Adv. Sci.*, 2024, **11**, 2308101.
64 S. Jiang, *et al.*, *Nat. Commun.*, 2023, **14**, 5455.
65 J. Miao and A. C. H. Tsang, *Adv. Sci.*, 2024, **11**, 2405641.
66 B. A. Grzybowski, H. A. Stone and G. M. Whitesides, *Nature*, 2000, **405**, 1033–1036.
67 J. Miao, *Sens. Actuators, A*, 2024, **368**, 115104.
68 J. Miao, S. Sun, T. Zhang, G. Li, H. Ren and Y. Shen, *ACS Appl. Mater. Interfaces*, 2022, **14**, 50296–50307.
69 K. Ichimura, S. K. Oh and M. Nakagawa, *Science*, 2000, **288**, 1624–1626.
70 G. Kwon, *et al.*, *Nat. Commun.*, 2017, **8**, 14968.
71 J. Lv, *et al.*, *Nature*, 2016, **537**, 179–184.
72 J. Miao, T. Zhang, G. Li, D. Guo, S. Sun, R. Tan, J. Shi and Y. Shen, *Engineering*, 2023, **23**, 170–180.
73 S. Liu, *et al.*, *Nat. Phys.*, 2025, **21**, 808–816.
74 H. Zhu, *et al.*, *Sci. Adv.*, 2025, **11**, eadv6314.
75 Y. Xue, J. Markmann, H. Duan, J. Weissmüller and P. Huber, *Nat. Commun.*, 2014, **5**, 4237.

76 M. K. Chaudhury, A. Chakrabarti and S. Daniel, *Langmuir*, 2015, **31**, 9266–9281.
77 J. Miao, J. Li and A. C. H. Tsang, *Nano Lett.*, 2025, **25**, 12495–12502.
78 H. Zhang, F. Wang and Z. Guo, *Adv. Colloid Interface Sci.*, 2024, **325**, 103097.
79 Y. Zhang, *et al.*, *Adv. Mater.*, 2021, **34**, 2108567.
80 D. Wu, *et al.*, *Adv. Mater.*, 2020, **32**, 2005039.
81 C. Li, C. Yu, D. Hao, L. Wu, Z. Dong and L. Jiang, *Adv. Funct. Mater.*, 2018, **28**, 1707490.
82 M. Liu, S. Wang and L. Jiang, *Nat. Rev. Mater.*, 2017, **2**, 17036.
83 W. Miao, Y. Tian and L. Jiang, *Acc. Chem. Res.*, 2022, **55**, 1467–1479.
84 T. Young, *Philos. Trans. R. Soc. London*, 1805, **95**, 65–87.
85 D. Bonn, J. Eggers, J. Indekeu, J. Meunier and E. Rolley, *Rev. Mod. Phys.*, 2009, **81**, 739.
86 R. N. Wenzel, *Ind. Eng. Chem.*, 1936, **28**, 988–994.
87 A. B. D. Cassie and S. Baxter, *Trans. Faraday Soc.*, 1944, **40**, 546–551.
88 X. Zhang, Y. Lei, C. Li, G. Sun and B. You, *Adv. Funct. Mater.*, 2022, **32**, 2110830.
89 O. Tricinci, F. Pignatelli and V. Mattoli, *Adv. Funct. Mater.*, 2023, **33**, 2206946.
90 Y. Si, Z. Dong and L. Jiang, *ACS Cent. Sci.*, 2018, **4**, 1102–1112.
91 Y. Xiang, *et al.*, *Proc. Natl. Acad. Sci. U. S. A.*, 2020, **117**, 2282–2287.
92 C. G. L. Furmidge, *J. Colloid Sci.*, 1962, **17**, 309–324.
93 H. J. Butt, J. Liu, K. Koynov, B. Straub, C. Hinduja, I. Roismann, R. Berger, X. Li, D. Vollmer, W. Steffen and M. Kappl, *Curr. Opin. Colloid Interface Sci.*, 2022, **59**, 101574.
94 A. Ponomarenko, D. Queue and C. Clanet, *J. Fluid Mech.*, 2011, **666**, 146–154.
95 F. J. Higuera, A. Medina and A. Liñán, *Phys. Fluids*, 2008, **20**, 102102.
96 A. L. Ramos and R. L. Cerro, *Chem. Eng. Sci.*, 1994, **49**, 2395–2398.
97 Q. Wang, Y. He, X. Geng, Y. Hou and Y. Zheng, *ACS Appl. Mater. Interfaces*, 2021, **13**, 48292–48300.
98 K. Luan, M. He, B. Xu, P. Wang, J. Zhou, B. Hu, L. Jiang and H. Liu, *Adv. Funct. Mater.*, 2021, **31**, 2010634.
99 M. Lee, J. Oh, H. Lim and J. Lee, *Adv. Funct. Mater.*, 2021, **31**, 2011288.
100 Y. Zhang, *et al.*, *Sci. Adv.*, 2021, **7**, eabi7498.
101 J. Iturri, *et al.*, *Adv. Mater.*, 2015, **25**, 1499–1505.
102 M. Chakraborty, J. A. Weibel, J. A. Schaber and S. V. Garimella, *Adv. Mater. Interfaces*, 2019, **6**, 1900652.
103 E. Bormashenko, T. Stein, R. Pogreb and D. Aurbach, *J. Phys. Chem. C*, 2009, **113**, 5568–5572.
104 L. Feng, Y. Zhang, J. Xi, Y. Zhu, N. Wang, F. Xia and L. Jiang, *Langmuir*, 2008, **24**, 4114–4119.
105 S. Ben, T. Zhou, H. Ma, J. Yao, Y. Ning, D. Tian, K. Liu and L. Jiang, *Adv. Sci.*, 2019, **6**, 1900834.
106 D. Wang, J. Huang and Z. Guo, *Chem. Eng. J.*, 2020, **400**, 125883.
107 W. Barthlott and C. Neinhuis, *Planta*, 1997, **202**, 1–8.
108 L. Feng, S. Li, Y. Li, H. Li, L. Zhang, J. Zhai, Y. Song, B. Liu, L. Jiang and D. Zhu, *Adv. Mater.*, 2002, **14**, 1857–1860.
109 P. Wang, T. Zhao, R. Bian, G. Wang and H. Liu, *ACS Nano*, 2017, **11**, 12385–12391.
110 C. Chen, M. Liu, L. Zhang, Y. Hou, M. Yu and S. Fu, *ACS Appl. Mater. Interfaces*, 2019, **11**, 7431–7440.
111 C. Liu, J. Ju, Y. Zheng and L. Jiang, *ACS Nano*, 2014, **8**, 1321–1329.
112 M. Liu, S. Wang, Z. Wei, Y. Song and L. Jiang, *Adv. Mater.*, 2009, **21**, 665–669.
113 W. Rong, H. Zhang, T. Zhang, Z. Mao, X. Liu and K. Song, *Adv. Eng. Mater.*, 2021, **23**, 2000821.
114 Y. Cai, *et al.*, *Adv. Funct. Mater.*, 2013, **24**, 809–816.
115 A. R. Parker and C. R. Lawrence, *Nature*, 2001, **414**, 33–34.
116 T. J. Brodribb, D. Bienaimé and P. Marmottant, *Proc. Natl. Acad. Sci. U. S. A.*, 2016, **113**, 4865–4869.
117 F. Vollrath and D. T. Edmonds, *Nature*, 1989, **340**, 305–307.
118 F. Vollrath, *Rev. Mol. Biotechnol.*, 2000, **74**, 67–83.
119 Y. Liu, Z. Shao and F. Vollrath, *Nat. Mater.*, 2005, **4**, 901–905.
120 F. Vollrath, W. J. Fairbrother, R. J. P. Williams, E. K. Tillinghast, D. T. Bernstein, K. S. Gallagher and M. A. Townley, *Nature*, 1990, **345**, 526–528.
121 F. Vollrath and D. Porter, *Soft Matter*, 2006, **2**, 377–385.
122 E. Doblhofer, A. Heidebrecht and T. Scheibel, *Appl. Microbiol. Biotechnol.*, 2015, **99**, 9361–9380.
123 Y. Zheng, *et al.*, *Nature*, 2010, **463**, 640–643.
124 M. K. Chaudhury and G. M. Whitesides, *Science*, 1992, **256**, 1539–1541.
125 S. Daniel, M. K. Chaudhury and J. C. Chen, *Science*, 2001, **291**, 633–636.
126 X. Yu, H. Lai, H. Kang, Y. Liu, Y. Wang and Z. Cheng, *ACS Appl. Mater. Interfaces*, 2022, **14**, 6274–6282.
127 E. Lorenceau and D. Queue, *J. Fluid Mech.*, 2004, **510**, 29–45.
128 H. Chen, *et al.*, *Nature*, 2016, **532**, 85–89.
129 P. Comanns, *et al.*, *J. R. Soc., Interface*, 2015, **12**, 20150415.
130 L. Yang, *et al.*, *Science*, 2024, **384**, 1344–1349.
131 L. Shang, Y. Cheng and Y. Zhao, *Chem. Rev.*, 2017, **117**, 7964–8040.
132 Y. Si, C. Li, J. Hu, C. Zhang and Z. Dong, *Adv. Funct. Mater.*, 2023, **33**, 2301017.
133 Y. Tian, *et al.*, *Nat. Commun.*, 2017, **8**, 1080.
134 M. Du, Y. Zhao, Y. Tian, K. Li and L. Jiang, *Small*, 2016, **12**, 1000–1005.
135 A. Greiner and J. H. Wendorff, *Angew. Chem.*, 2007, **119**, 5770–5805.
136 H. Bai, J. Ju, R. Sun, Y. Chen, Y. Zheng and L. Jiang, *Adv. Mater.*, 2011, **23**, 3708–3711.
137 H. Dong, Y. Zheng, N. Wang, H. Bai, L. Wang, J. Wu, Y. Zhao and L. Jiang, *Adv. Mater. Interfaces*, 2016, **3**, 1500831.

138 X. He, *et al.*, *ACS Appl. Mater. Interfaces*, 2015, **7**, 17471–17481.
139 J. Ju, K. Xiao, X. Yao, H. Bai and L. Jiang, *Adv. Mater.*, 2013, **25**, 5937–5942.
140 J. Van Hulle, *et al.*, *Phys. Rev. Fluids*, 2021, **6**, 024501.
141 M. Cao, J. Ju, K. Li, S. Dou, K. Liu and L. Jiang, *Adv. Funct. Mater.*, 2014, **24**, 3235–3240.
142 J. Ju, X. Yao, S. Yang, L. Wang, R. Sun, Y. He and L. Jiang, *Adv. Funct. Mater.*, 2014, **24**, 6933–6938.
143 K. Li, J. Ju, Z. Xue, J. Ma, L. Feng, S. Gao and Lei Jiang, *Nat. Commun.*, 2013, **4**, 2276.
144 Z. Cui, *et al.*, *J. Mater. Chem. A*, 2025, **13**, 18870.
145 Y. Li, *et al.*, *Adv. Funct. Mater.*, 2022, **32**, 2201035.
146 Z. Wang, *et al.*, *Int. J. Extreme Manuf.*, 2025, **7**, 025505.
147 C. Li, H. Dai, C. Gao, T. Wang, Z. Dong and L. Jiang, *Proc. Natl. Acad. Sci. U. S. A.*, 2019, **116**, 12704–12709.
148 Z. Wang, Z. Zhan, L. Chen, G. Duan, P. Cheng, H. Kong, Y. Chen and H. Duan, *Sol. RRL*, 2022, **6**, 2101063.
149 T. Wang, Y. Si, H. Dai, C. Li, C. Gao, Z. Dong and L. Jiang, *Proc. Natl. Acad. Sci. U. S. A.*, 2020, **117**, 1890–1894.
150 S. Liu, C. Zhang, T. Shen, Z. Zhan, J. Peng, C. Yu, L. Jiang and Z. Dong, *Nat. Commun.*, 2023, **14**, 5934.
151 S. Liu, Z. Zhan, Y. Si, C. Yu, L. Jiang and Z. Dong, *Adv. Funct. Mater.*, 2023, **33**, 2212485.
152 X. Tang, P. Zhu, Y. Tian, X. Zhou, T. Kong and L. Wang, *Nat. Commun.*, 2017, **8**, 14831.
153 Z. Cheng, C. Li, C. Gao, C. Zhang, L. Jiang and Z. Dong, *Sci. Adv.*, 2023, **9**, eadi5990.
154 S. Zhang, M. Chi, J. Mo, T. Liu, Y. Liu, Q. Fu, J. Wang, B. Luo, Y. Qin, S. Wang and S. Nie, *Nat. Commun.*, 2022, **13**, 4168.
155 H. Geng, H. Bai, Y. Fan, S. Wang, T. Ba, C. Yu, M. Cao and L. Jiang, *Mater. Horiz.*, 2018, **5**, 303–308.
156 B. Zhao, J. S. Moore and D. J. Beebe, *Science*, 2001, **291**, 1023–1026.
157 A. I. Shallan, Y. Tavares, M. N. Kashani, M. C. Breadmore and C. Priest, *Angew. Chem.*, 2021, **133**, 2686–2689.
158 D. J. Guckenberger, T. E. Groot, A. M. D. Wan, D. J. Beebea and E. W. K. Young, *Lab Chip*, 2015, **15**, 2364–2378.
159 J. Yu, *et al.*, *Nat. Biomed. Eng.*, 2019, **3**, 830–841.
160 Q. Zhang, S. Feng, L. Lin, S. Mao and J. M. Lin, *Chem. Soc. Rev.*, 2021, **50**, 5333–5348.
161 X. Liu, B. Li, Z. Gu and K. Zhou, *Small*, 2023, **19**, 2207640.
162 U. Hermens, *et al.*, *Appl. Surf. Sci.*, 2017, **418**, 499–507.
163 M. Xie, *et al.*, *Small*, 2023, **19**, 2300047.
164 J. Miao and A. C. H. Tsang, *ACS Nano*, 2025, **19**(5), 5829–5838.
165 Y. Si, T. Wang, C. Li, C. Yu, N. Li, C. Gao, Z. Dong and L. Jiang, *ACS Nano*, 2018, **12**, 9214–9222.
166 Z. Liu, Z. Zhan, T. Shen, N. Li, C. Zhang, C. Yu, C. Li, Y. Si, L. Jiang and Z. Dong, *Nat. Commun.*, 2023, **14**, 4128.
167 S. Sun, J. Miao, R. Tan, T. Zhang, G. Li and Y. Shen, *Adv. Funct. Mater.*, 2022, **33**, 2209769.
168 S. Sun, Y. Zhang, S. Wu and L. Wang, *Adv. Mater.*, 2024, **36**, 2209769.
169 R. Erp, R. Soleimanzadeh, L. Nela, G. Kampitsis and E. Matioli, *Nature*, 2020, **585**, 211–216.
170 W. Li, S. Yang, Y. Chen, C. Li and Z. Wang, *Nat. Commun.*, 2023, **14**, 3996.
171 G. Dupeux, *et al.*, *Sci. Rep.*, 2014, **4**, 5280.
172 A. Bouillant, *et al.*, *Nat. Phys.*, 2018, **14**, 1188–1192.
173 S. Shen, *et al.*, *Lab Chip*, 2017, **17**, 3578–3591.
174 M. Saito, *et al.*, *Proc. Natl. Acad. Sci. U. S. A.*, 2024, **121**, e2306182121.
175 A. Groisman, *et al.*, *Phys. Rev. Lett.*, 2004, **92**, 094501.
176 E. K. Sackmann, A. L. Fulton and D. J. Beebe, *Nature*, 2014, **507**, 181–189.
177 Y. Yu, H. Wen, J. Ma, S. Lykkemark, H. Xu and J. Qin, *Adv. Mater.*, 2014, **26**, 2494–2499.
178 Y. Ma, J. Z. Pan, S. P. Zhao, Q. Lou, Y. Zhu and Q. Fang, *Lab Chip*, 2016, **16**, 4658–4665.
179 L. Keiser, P. Marmottant and B. Dollet, *J. Fluid Mech.*, 2022, **948**, A52.
180 Y. Zeng, *et al.*, *Nat. Chem. Eng.*, 2024, **1**, 149–158.
181 P. Zhu, T. Kong, X. Tang and L. Wang, *Nat. Commun.*, 2017, **8**, 15823.
182 C. Soitu, A. Feuerborn, C. Deroy, A. A. Castrejón-Pita, P. R. Cook and E. J. Walsh, *Sci. Adv.*, 2019, **5**, eaav8002.
183 E. J. Walsh, *et al.*, *Nat. Commun.*, 2017, **8**, 816.
184 C. Li, *et al.*, *Sci. Adv.*, 2020, **6**, eaay9919.
185 K. Luan, M. He, B. Xu, P. Wang, J. Zhou, B. Hu, L. Jiang and H. Liu, *Adv. Funct. Mater.*, 2021, **31**, 2010634.
186 Y. J. Chen, *et al.*, *ACS Appl. Mater. Interfaces*, 2024, **16**, 36840–36850.
187 K. C. Park, P. Kim, A. Grinthal, N. He, D. Fox, J. C. Weaver and J. Aizenberg, *Nature*, 2016, **531**, 78–82.
188 Y. Zhang, Z. Dong, C. Li, H. Du, N. X. Fang, L. Wu and Y. Song, *Nat. Commun.*, 2020, **11**, 4685.
189 C. Yu, L. Zhang, Y. Ru, N. Li, C. Li, C. Gao, Z. Dong and L. Jiang, *ACS Nano*, 2018, **12**, 11307–11315.
190 K. Yang, *et al.*, *Adv. Mater.*, 2025, **37**, 2417337.
191 B. Zhang, K. Yang, X. Yu, J. Zhang, Z. Dong, R. Fang and L. Jiang, *Adv. Funct. Mater.*, 2025, **35**, 2422552.
192 C. Yang, W. Li, Y. Zhao and L. Shang, *Proc. Natl. Acad. Sci. U. S. A.*, 2024, **121**, e2402331121.
193 C. Yang, Y. Yu, L. Shang and Y. Zhao, *Nat. Chem. Eng.*, 2024, **1**, 87–96.
194 B. Zhang, *et al.*, *Nature*, 2024, **628**, 84–92.
195 M. Cao, *et al.*, *Matter*, 2024, **7**, 3053–3068.
196 Y. Zhang, *et al.*, *Nat. Chem. Eng.*, 2024, **1**, 472–482.
197 N. A. Dudukovic, *et al.*, *Nature*, 2021, **595**, 58–65.
198 S. Wu, S. Sun, J. Ye, L. Wang and Y. Zhang, *Adv. Mater.*, 2025, 2503840.
199 R. Mcnair, *et al.*, *Phys. Rev. Lett.*, 2025, **134**, 034001.
200 F. T. Coleto, *et al.*, *Phys. Rev. Fluids*, 2018, **3**, 100507.
201 H. Zhao, *et al.*, *Adv. Funct. Mater.*, 2024, **34**, 2407654.
202 X. Lin, H. Wang, Y. Wu and S. He, *ACS Nano*, 2025, **19**, 25986–25998.

203 C. Zhang, *et al.*, *Nano Lett.*, 2025, **25**, 11618–11625.
204 J. Miao and S. Sun, *J. Magn. Magn. Mater.*, 2023, **586**, 171160.
205 D. Mark, S. Haeberle, G. Roth, F. Stetten and R. Zengerle, *Chem. Soc. Rev.*, 2010, **39**, 1153–1182.
206 E. K. Sackmann, A. L. Fulton and D. J. Beebe, *Nature*, 2014, **507**, 181–189.
207 S. Wu, *et al.*, *Appl. Phys. Lett.*, 2023, **122**, 174101.
208 P. Zhu and L. Wang, *Lab Chip*, 2017, **17**, 34–75.
209 Q. Deng, *et al.*, *Nat. Commun.*, 2025, **16**, 4601.